# Damage investigation of blast loaded UHPFRC panels with optimized mixture design using advanced material models

Mohammad Momeni [a], Demetris Demetriou [b], Loucas Papadakis [c,d], Chiara Bedon [a,*], Michael F. Petrou [b], Demetris Nicolaides [c,d]

[a] *University of Trieste, Department of Engineering and Architecture, Trieste, Italy*
[b] *University of Cyprus, Department of Civil & Environmental Engineering, Nicosia, 1303, Cyprus*
[c] *Frederick Research Center, 7 Filokyprou Str. Pallouriotisa, Nicosia, 1036, Cyprus*
[d] *Frederick University, Department of Civil Engineering, 7 Y. Frederickou Str. Pallouriotisa, Nicosia, 1036, Cyprus*

## ARTICLE INFO

## ABSTRACT

The increasing use of innovative materials in blast- and impact-resistant structures underscores the demand for robust simulation and design methods. Concrete, especially Ultra High Performance Fiber Reinforced Concrete (UHPFRC), has emerged as a key player in this domain. The present study delves into the damage investigation and dynamic response assessment of blast loaded UHPFRC panels with optimized mixture design (microsilica content, water curing conditions, and fibre proportions). The so-assembled UHPFRC material is calibrated and validated, adjusting parameters from experimental results addressing the tensile and compressive behaviours of material based on standard experimental methods. The investigation navigates through experimental and numerical challenges, emphasizing the limitations of applying available models to UHPFRC, and necessitates recalibration for optimal alignment with experimental results. An in-depth numerical analysis using LS-DYNA software is also carried out, aiming to understand the dynamic behaviour of UHPFRC panels under blast loading and performing a comparative analysis between UHPFRC and normal strength concrete (NSC) panels with and without reinforcement, emphasizing the superior performance of UHPFRC. Furthermore, the study addresses the importance of determining the minimum thickness for UHPFRC panels as protective barriers. This involves a specific strategy based on regulations and considering minimal damage to the panel, leading to the proposal of an empirical formulation. Additionally, a sensitivity analysis has been conducted to identify the influential parameters on the response of the panel. The findings of this study revealed that modelling the UHPFRC material using finite element analysis and employing advanced material models yield promising outcomes. Moreover, the proposed empirical formulation demonstrates a good level of accuracy and efficiency in predicting the minimum thickness for UHPFRC panels under blast conditions. The results of the sensitivity analysis also indicate that explosive charge weight, standoff distance, and panel thickness are the most critical parameters. These insights contribute to a comprehensive understanding of UHPFRC dynamic behaviour in blast conditions, offering valuable considerations for future applications and design implementations in this evolving field.

## 1. Introduction

In the last decades, the use of innovative materials for blast and impact resistant structures has intensively increased in construction which highlighted the importance and need of appropriate simulation and design methods for these kinds of structures under extreme dynamic loads [1,2]. Concrete can be considered as an effective and widely used material in construction industry and in the design of structures under different loads like impact and blast [3–5]. The compressive strength of normal strength concrete (NSC) is much greater than its tensile strength, indicating that concrete weakness in tension needs enhancement, which can be achieved using different strategies. In comparison to NSC, Ultra High Performance Concrete (UHPC) possesses an elevated concentration of cementitious materials and a reduced water-to-cementitious material ratio. Additionally, it contains a higher proportion of fine mineral admixture, such as silica fume, and employs highly efficient

superplasticizers. Typically, UHPC excludes coarse aggregates to enhance material homogeneity, subsequently improving compressive strength. Longitudinal reinforcement bars as well as fibres can be used to increase the tensile strength of concrete significantly. In other words, researchers continually endeavour to discover innovative methods for enhancing the behaviour of concrete materials and mitigating their defects under various types of loading [6–8]. In this regard, the incorporation of high-strength fibres in UHPC is a common practice to mitigate brittleness which leads to Ultra High Performance Fiber Reinforced Concrete (UHPFRC) where the fibre types often used include high carbon steel, Polyvinyl Alcohol (PVA), glass, carbon or a combination of these types or others. UHPFRC shows good potential as a construction material for protective structures, owing to its outstanding mechanical characteristics, such as high strength, energy absorption capacity, and distinctive strain hardening/softening behaviour [9]. Furthermore, UHPFRC can be combined with other types of materials, such as thermal-resistant materials, in a composite structure (or material) to create a multi-objective structure (or material) that not only resists thermal effects but also exhibits highly promising behaviour under dynamic loads like blast and impact as well as seismic. However, the method of connecting different layers in a component is also important, and various materials, numerical, and experimental methods have been proposed in the literature for this issue [10,11]. Numerous research studies have been conducted to investigate the behaviour of UHPC and UHPFRC under various loadings. Several experimental studies can be found in the literature, where different structures made from these materials have been investigated under blast and impact [12–15]. Such experimental works help to investigate the behaviour of these materials under real impulsive loads in terms of energy absorption, damage, pattern of crack propagation, etc., in comparison to normal concrete. They help also to develop analytical and numerical methods based on different software packages [16–20]. Among others, LS-DYNA encompasses different material properties that can be used for concrete, and several efforts have been made to formalize the behaviour of concrete material by employing appropriate models [21,22]. Although these models may be suitable for traditional concrete materials, it is essential to exercise caution when applying them to UHPFRC. In other words, using these models with their default parameters may not be suitable for UHPFRC, and it becomes necessary to adapt and calibrate them based on experimental data to achieve the best possible alignment between experimental and numerical results. Several studies have been carried out in the literature that mainly focused on this issue and made many efforts to calibrate these models, especially Mat_72R3 and Mat_159 for UHPC material subjected to different types of impulsive loadings like blast and impact [20,23–29], and their applications in different kind of concrete structures like beam, column, panel, etc. [30–47]. In addition, some research studies can be found in the literature that has been dedicated to finding the response of such structures under seismic loads [48,49], environmental [50], and fire loading [51,52]. Nevertheless, it is essential to highlight that when dealing with a novel material mixture tailored for a specific purpose, recalibration becomes necessary. This involves adjusting the input parameters of these models based on experimental results to achieve optimal performance, which can be done based on standard methods reported in the literature like single element strategy [20,36,53,54].

On the other hand, according to the literature, one of the ways to minimize the impact of the blast, is providing a suitable standoff distance for a structure. According to the UFC3-340-02 [55] code, a minimum standoff distance of 15 ft (4.57 m) is a good choice for any structure to resist the effect of blast loading. However, this value may not work for all structures due to different material properties, geometry, explosive charge weight, etc. So, one thing that can be done is to estimate this value by different strategies that reported in the literature [56,57]. On the other hand, the UHPFRC panel can be constructed as a prefabricated member off-site or on-site (with specific width and height but different thicknesses) and then moved to be connected to a structure as a protective barrier. In this case, providing a strategy to find the minimum thickness of the panel to resist the blast load is of interest, which can be intelligently determined by utilizing the methods specified in the regulations and by employing the minimum damage created in the panel. In existing literature, several research studies have focused on determining the efficiency of protective barrier panels under fragment and projectile impacts to find the depth of penetration [58–62]. UFC-3-340-02 [55] provides different formulations for various structures subjected to fragments, typically relying on calculating the penetration depth of fragments after impact as a function of striking velocity, fragment diameter, shape, and other factors. To ensure panel safety, the thickness of the designed structures should be equal to or greater than the penetration depth of the impactor. Despite various studies addressing their behaviour under such loads in terms of deflection, strain, damage patterns, etc., which are discussed earlier, however, there is a gap in the literature regarding the minimum required thickness of UHPFRC panels for blast loading, which is another contribution of this research study.

In addition to what is mentioned above, and notwithstanding the array of experimental and numerical challenges in the application of UHPFRC in construction, a significant obstacle in UHPFRC production lies in concurrently optimizing various input parameters to achieve superior properties at minimal cost and environmental impact. Recent research studies [63–69] have focused on reducing UHPFRC's carbon footprint and material costs, exploring methods such as decreasing cement content, utilizing supplementary cementitious materials, substituting standard sand, employing hybrid fibre systems, and adopting standard curing for reduced energy consumption. Building on prior work by certain authors within this study, an optimal mixture of UHPFRC was determined and proposed [7,70]. This mixture includes considerations such as microsilica content, water curing temperature and duration, and proportions of mono-fibre steel, hybrid steel, and PVA fibres. The proposed mixture not only optimizes mechanical, physical, and durability considerations but has also undergone experimental validation for its stability under short-duration loads. While the suggested optimal mix design for concrete demonstrates commendable performance, a more thorough investigation is needed, particularly under explosive loading scenarios, which is discussed in this study.

In light of the outlined objectives, this study sets to address the critical knowledge gap in understanding the dynamic response of UHPFRC under blast loading conditions through advanced numerical simulations using LS-DYNA. In this regard, building upon previous research endeavours, an optimized mix design for UHPFRC panels is implemented, with the primary objective of numerically analysing the applicability of this material for panels under explosive loading conditions. The optimized UHPFRC and its corresponding mix design are presented concisely, along with experimental findings addressing the tensile and compressive behaviours. Subsequently, the investigation extends to a comprehensive numerical examination of the UHPFRC, utilizing the Mat_72Rel3 material model based on LS-DYNA software. This phase involves a comprehensive effort to calibrate and validate the material model and adjustment of its input parameters to align seamlessly with observed experimental results, followed by the validation of numerical modelling for blast response simulations using multi-material arbitrary Lagrangian-Eulerian (MM_ALE) and load-blast-enhanced (LBE) techniques. The scope broadens further with a comparative analysis of panel responses made from NSC and UHPFRC, with and without reinforcement, assessing the superior performance of UHPFRC material. Additionally, the numerical modelling extends to determining the minimum required thickness of the UHPFRC panel, ensuring effective resistance against blast loads while containing damage within acceptable limits as low damage. Finally, the study concludes with a sensitivity analysis, identifying the most influential parameters in the numerical model, thus contributing to a comprehensive understanding of the dynamic behaviour and blast response of UHPFRC structures for future applications and design considerations.

**Table 1**
UHPFRC mixture.

| Constituent | Content |
|---|---|
| Cement | 880 (kg/m$^3$) |
| Microsilica | 220 (kg/m$^3$) |
| Standard Sand | 833 (kg/m$^3$) |
| Water | 176 (kg/m$^3$) |
| Superplasticizer | 67 (kg/m$^3$) |
| Steel fibres 6 mm | 120 (kg/m$^3$) |
| Steel fibres 13 mm | 120 (kg/m$^3$) |
| PVA fibres | 13 (kg/m$^3$) |
| Water/Binder | 0.16 (−) |

## 2. Material properties and experimental results

### 2.1. UHPFRC mixture

The UHPFRC mixture used in this research consists of an optimized version of the mixture detailed in Nicolaides et al. [7], tailored to enhance its mechanical properties, such as compressive, tensile, and flexural strength, modulus of elasticity, and specific fracture energy. This optimization involved adjustments to microsilica content, water-to-binder (W/B) ratios, and the proportions and types of fibres, including steel and hybrid steel and PVA fibres. For detailed insights into the optimization procedure, readers are directed to the study of Demetriou et al. [70]. Table 1 presents the composition of the optimized mixture.

### 2.2. Experimental tests and results

In this study, the experimental results of the proposed UHPFRC mixture under both compressive and tensile axial load have been used to calibrate the numerical modelling in predicting the behaviour of UHPFRC under applied load. The experimental tests were carried out at the University of Cyprus, and a summary of the tests and their results are presented in Table 2. The obtained stress-strain curves for both compressive and tensile behaviour are illustrated in Fig. 1.

## 3. UHPFRC constitutive model

In both civil and military applications, concrete is a frequently used construction material. Although there are practically considerable varieties of concrete, the majority of them can be described by a single parameter called the uniaxial unconfined compressive strength ($f'_c$). Although this single parameter cannot adequately describe every aspect of concrete material, engineers are frequently asked to conduct analyses involving concrete when no data is available to characterize the concrete besides from $f'_c$. In this regard, as an example, the Karagozian & Case Concrete (K&C) model has been proposed in the literature [22,71] in order to capture the behaviour of concrete especially under extreme dynamic loads. Originally, this material model was proposed and calibrated for a normal-strength concrete with an unconfined compressive strength of 45.6 MPa and has the ability to generate model parameters solely based on the unconfined uniaxial compressive strength. However, the composition of UHPFRC differs significantly from that of normal strength concrete; hence, using this model material for UHPFRC without any modification leads to inaccurate results. There are several research studies in the literature that have been dedicated to the modification of the K&C model material and its calibration for UHPC under extreme dynamic loads like blast and impact [20,26]. In this research study, the proposed formulations of Zhang et al. [26] are implemented for the UHPFRC material that are summarized in the following, but some of its parameters are adjusted based on the available experimental results

**Table 2**
Results of axial tests for UHPFRC.

| Material Property | Value |
|---|---|
| Density (Kg/m$^3$) | 2270 |
| Compressive strength (MPa) from Cubes (100 mm × 100 mm × 100 mm) | 154.55 |
| Compressive strength (MPa) from cylindrical specimens (radius = 100 mm × height = 200 mm) | 115.23 |
| Modulus of Elasticity (GPa) from compression tests | 55.72 |
| Poisson's ratio | 0.24 |
| Tensile strength (MPa) from prismatic beams (100 mm × 50 mm × 500 mm) | 8.9 |

(this will be later discussed in detail). The reason for selecting this model is that the model was performed based on many experimental tests from the literature, that also contains fibre reinforced specimens.

### 3.1. Failure surface parameters

In the K&C model material, the failure surfaces are defined in terms of the principal stress difference. The three failure surfaces, namely maximum failure surface $\Delta_{\sigma m}$, residual failure surface $\Delta_{\sigma r}$, and initial yield failure surface $\Delta_{\sigma y}$, can be separately defined as following a function of compressive strength of UHPFRC.

$$\Delta\sigma_m = a_0 + \frac{P}{a_1 + a_2 P}$$
$$\Delta\sigma_r = \frac{P}{a_{1f} + a_{2f}P} \tag{1}$$
$$\Delta\sigma_y = a_{0y} + \frac{P}{a_{1y} + a_{2y}P}$$

where P is the pressure, and $a_0$, $a_1$, $a_2$, $a_{1f}$, $a_{2f}$, $a_{0y}$, $a_{1y}$, and $a_{2y}$ are the failure surface parameters that are defined as below:

$$a_0 = 0.3444f'_c, a_1 = 0.4463, a_2 = 0.1847/f'_c$$
$$a_{1f} = 0.4417, a_{2f} = 0.1737/f'_c \tag{2}$$
$$a_{0y} = 0.2182f'_c, a_{1y} = 0.6250, a_{2y} = 0.5433/f'_c$$

where $f'_c$ is the compressive strength of UHPFRC material.

### 3.2. Strain rate effect

Under extreme dynamic loading with a high strength rate, the strength of concrete material will increase significantly and thus affects the structural performance. The strain rate effects can be considered in the modelling by using a dynamic increase factor (DIF) which is defined as the ratio between dynamic and quasi-static strengths for both compression and tension behaviours. In the following, the DIF equations for both compression and tension behaviour are summarized.

- Equations for DIF in compression (DIF$_c$)

$$DIF_c = \left(\frac{\dot{\varepsilon}_c}{\dot{\varepsilon}_{co}}\right)^{\alpha_c}, \dot{\varepsilon}_c \le 60s^{-1} DIF_c = \gamma_c \left(\frac{\dot{\varepsilon}_c}{\dot{\varepsilon}_{co}}\right)^{\beta_c}, \dot{\varepsilon}_c > 60s^{-1} \tag{3}$$

Where $\dot{\varepsilon}_{co}$ = 30e-6 s$^{-1}$ is the compressive quasi-static strain rate; the other parameters are defined as follows:

$$\alpha_c = \frac{1}{0.975 + 0.877f'_c} \log \gamma_c = 6.301\alpha_c - 1.890\beta_c = 0.3 \tag{4}$$
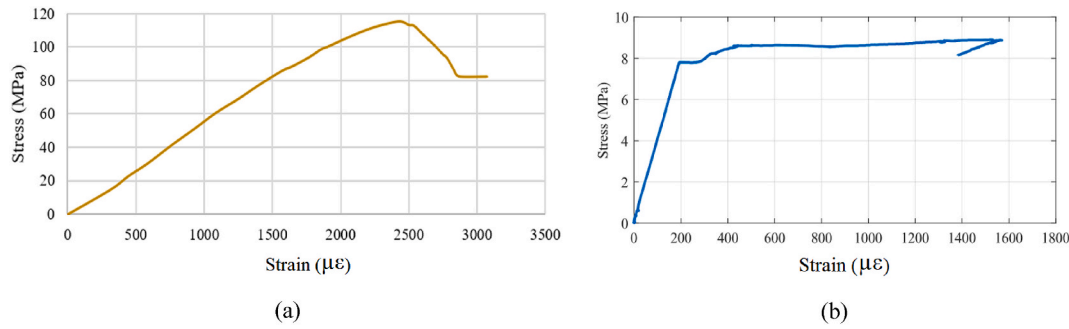
Fig. 1. Stress–strain curve in: (a) compression from cylindrical specimens with radius = 100 mm × height = 200 mm, (b) tension from prismatic beams (100 mm × 50 mm × 500 mm).

- Equations for DIF in tension (DIF$_t$)

$$DIF_t = \left(\frac{\dot{\varepsilon}_t}{\dot{\varepsilon}_{to}}\right)^{\alpha_t}, \dot{\varepsilon}_t \leq \dot{\varepsilon}_{t\_TR} s^{-1} \qquad DIF_t = \gamma_t \left(\frac{\dot{\varepsilon}_t}{\dot{\varepsilon}_{to}}\right)^{\beta_t}, \dot{\varepsilon}_t > \dot{\varepsilon}_{t\_TR} s^{-1} \qquad (5)$$

where $\dot{\varepsilon}_{to}$ = 1.0e-6 s$^{-1}$ is the tensile quasi-static strain rate; the other parameters are defined as follows:

$$\dot{\varepsilon}_{t\_TR} = \begin{cases} 2s^{-1}, f_c' \leq 140 MPa \\ 10s^{-1}, f_c' > 140 MPa \end{cases} \quad \alpha_t = \frac{1}{1 + 0.8 f_c'} \log \gamma_t = \begin{cases} 6.301\alpha_t - 3.151, f_c' \leq 140 MPa \\ 7\alpha_t - 3.5, f_c' > 140 MPa \end{cases} \quad \beta_t = 0.5 \qquad (6)$$

It is important to emphasize the necessity of introducing a cut-off value in DIF equations to prevent the overestimation of DIFs due to the inertia effect at high strain rates. Accordingly, DIF cutoff values are adopted to be established at strain rates of 300 s$^{-1}$ in compression and 100 s$^{-1}$ in tension based on [26].

### 3.3. Equation of state

To describe the volumetric behaviour of concrete in the K&C model material, the equation of state (EOS) should be defined in LS-DYNA. To this aim, tabulated pressure values in terms of volumetric strain values should be provided based on the following equation:

$$P = C(\mu) + \gamma T(\mu)E \qquad (7)$$

where $P$ is the pressure and $\mu$ is the volumetric strain. The first term on the right, $C(\mu)$, is the tabulated mechanical pressure at 0 K isotherm. The second term on the right, $\gamma T(\mu)E$, describes the thermally induced pressure with $\gamma$ as the specific heat modulus, $E$ as the internal energy per unit reference volume, and $T(\mu)$ as the tabulated parameter related to temperature. It should be noted that the temperature-related variation of hydrostatic pressure (i.e. $\gamma T(\mu)E$) can be neglected according to Refs. [72–74] for UHPFRC under blast and impact loads. However, for the case of thermal load, appropriate values according to experiments or literature should be selected, and a sensitivity analysis can also be done on the effect of this part on the outputs.

In this research study, the *EOS_TABULATED_COMPACTION card is used to define the equation of state for UHPFRC and the reference input parameters are adopted from Ref. [24] for UHPC and listed in Table 3. This reference was selected for its unique feature of having parametric values proposed. In contrast to most studies where specific values are provided exclusively for internal use, this particular reference showcases a comprehensive formula for their calculation. This quality lends itself to

significant advantages, particularly when dealing with diverse input parameters like compressive strength. Furthermore, these values can be easily adjusted to account for changes in the relevant input parameters, thereby enhancing their flexibility and utility. It is also worth mentioning that from the origin to the first data point, the curve's initial portion is the linear response represented by the elastic bulk module (K), which is derived from the elastic modulus, E, using the following expression [38,75]:

$$K = \frac{E}{3(1 - 2\nu)} = 2131.67\sqrt{f_c'}(MPa) \qquad (8)$$

where $\nu$ is Poisson ratio, K is bulk modulus and E is the elastic modulus of UHPFRC. For other input parameters of the EOS card, the default values of the LS-DYNA are adopted. It should be noted that the values of volumetric strain should be imported with negative signs in the EOS of LS-DYNA.

### 3.4. Failure surface interpolation function

Due to the incorporation of fibres, the hardening and softening characteristics of UHPFRC differ from those of NSC. The LS-DYNA default values for the failure surface interpolation function η(λ) are derived from NSC data and are consequently inappropriate for UHPFRC. The failure surface is defined by the function η(λ), where the scale factor (η) varies with the accumulated effective plastic strain parameter (λ). To define η(λ), thirteen (λ, η) pairs can be inputted to define this function, with values not provided by the data sets determined by interpolation.

**Table 3**
Calibrated EOS parameters for UHPFRC [24].

| i | 1 | 2 | 3 | 4 | 5 | 6 | 7 | 8 | 9 | 10 |
|---|---|---|---|---|---|---|---|---|---|---|
| μ$_i$ | 0 | 0.0015 | 0.0043 | 0.0101 | 0.0305 | 0.0513 | 0.0726 | 0.0943 | 0.174 | 0.208 |
| K$_i$ (MPa) | K | K | 1.014K | 1.065K | 1.267K | 1.47K | 1.672K | 1.825K | 4.107K | 5K |
| P$_i$ (MPa) | 0 | μ$_2$K | 3μ$_2$K | 7μ$_2$K | 14μ$_2$K | 21μ$_2$K | 30μ$_2$K | 42μ$_2$K | 127μ$_2$K | 195μ$_2$K |

**Table 4**
Tabulated values for different η-λ functions.

| Default η-λ function | | Markovich et al. η-λ function | | Proposed η-λ function | |
|---|---|---|---|---|---|
| λ | η | λ | η | λ | η |
| 0.0 | 0.000 | 0.0 | 0.000 | 0.0 | 0.000 |
| 1.56E-06 | 0.666 | 2.80E-05 | 0.700 | 1.48E-05 | 0.666 |
| 9.78E-06 | 0.907 | 5.00E-05 | 0.900 | 2.99E-05 | 0.907 |
| 9.66E-06 | 0.934 | 9.00E-05 | 1.000 | 3.98E-05 | 0.950 |
| 2.35E-05 | 0.968 | 1.70E-04 | 0.900 | 5.68E-05 | 0.990 |
| 4.68E-05 | 0.992 | 3.00E-04 | 0.750 | 8.84E-05 | 1.000 |
| 7.02E-05 | 0.987 | 5.50E-04 | 0.540 | 1.20E-04 | 0.970 |
| 8.89E-05 | 0.966 | 1.00E-03 | 0.330 | 3.30E-04 | 0.600 |
| 1.03E-04 | 0.934 | 1.63E-03 | 0.170 | 4.70E-04 | 0.350 |
| 1.31E-04 | 0.868 | 2.50E-03 | 0.090 | 1.00E-03 | 0.170 |
| 1.88E-04 | 0.767 | 3.50E-03 | 0.032 | 1.63E-03 | 0.100 |
| 2.31E-04 | 0.669 | 7.00E-03 | 0.005 | 2.50E-03 | 0.010 |
| 5.70E-04 | 0.006 | 1.00E+00 | 0.000 | 7.50E-03 | 0.006 |
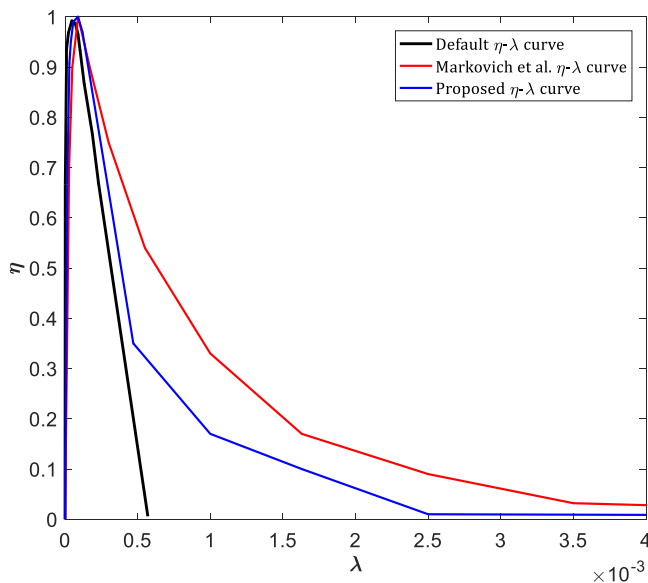


**Fig. 2.** Comparison of different η-λ functions.

The parameter λ is a function of $b_1$ (compressive damage scaling parameter) for P > 0 in the compressive region, and $b_2$ (the tensile damage scaling exponent) in the tension region (P ≤ 0) (more details can be found in Refs. [19,20,26]). These parameters govern the uniaxial compressive and tensile damage accumulation rates of concrete during the softening stage. It's important to note that changing the values of $b_1$ and $b_2$ can affect the λ-η function, requiring adjustments to align with experimental data since these parameters are dependent on each other. In this study, the effect of three different η(λ) function are investigated on the behaviour of the proposed concrete mixture. These functions are: I) the default values for the failure surface interpolation function η(λ) in LS-DYNA, II) the modified η-λ function proposed in Markovich et al. [26, 29], and III) an η(λ) function that is proposed here in this study for the examined material (which later will be discussed). The tabulated values for the three η-λ functions are presented in Table 4 and a comparison figure is also shown in Fig. 2.

According to Fig. 2, it can be seen that η increases from 0 to 1 as λ increases from 0 to $λ_m$ (the value of λ at η = 1 corresponds to maximum failure surface) during the hardening stage, and decreases from 1 to 0 during the softening stage. It is noticeable that during the hardening phase (0 < λ ≤ $λ_m$ and 0 < η ≤ 1), the interpolation function undergoes a slightly slower evolution to account for the distinct hardening behaviours exhibited by NSCs and UHPFRCs. In the softening phase (λ > $λ_m$ and η < 1), the adjusted η-λ relationship exhibits a more gradual decrease compared to the default values. This modification reflects a

more ductile response attributed to the presence of fibres in UHPFRCs. It should be noted that $λ_m$ is the value of λ at η = 1. It is important to note that, in the numerical simulation models based on K&C model, which are performed in this study, the same η-λ function is applied for both compression and tension.

## 4. Numerical modelling and calibration of the constitutive model

In the pursuit of evaluating the efficacy of the Mat_72Rel3 in characterizing the response of UHPFRC under axial loads, a thorough examination is conducted in this section using LS-DYNA software. A crucial point of consideration is that, although the formulation of [26] has been implemented in this study, efforts have been made to adjust some of its damage parameters (including $b_1$, $b_2$ and η-λ function that will be later discussed in more detail) based on the current experimental results performed in this study, aiming to achieve the best possible match between experimental and numerical results, for both tensile and compressive behaviours.

In the case of compressive behaviour, the experimental setup (Fig. 3a) involves the incorporation of two steel plates positioned at the top and bottom of the specimen, enabling the application of axial load. It's essential to highlight that the compressive axial load is gradually applied to the concrete specimen at a controlled rate of 0.015 mm/min to simulate quasi-static loading conditions. The numerical modelling approach employs solid elements for both the concrete specimen and the upper and lower steel plates. The bottom steel plate is used as a support condition for concrete specimen (all translational and rotational degrees of freedom are constrained), while the upper steel plate is used to apply the axial load on the specimens (translational degree of freedom in the z-direction is released and other degrees of freedom are constrained). For steel plates, a rigid material model (Mat_Rigid) is used, while concrete utilizes the material model Mat_72Rel3. Input parameters for the concrete material model and its equation of state have been calculated based on the procedure provided in preceding sections and integrated into the LS-DYNA software. Considering the extremely low rate at which the load is applied to the concrete specimen (i.e., 0.015 mm/min), the effects of strain rate in this scenario are considered inactive. To account for the interaction between the upper and lower steel plates and the concrete specimen, the CONTACT_AUTOMATIC_SURFACE_TO_SURFACE command is employed. This command, which is penalty-based, manages the interactions between different components of a specimen by preventing penetration in the normal direction and applying a friction model in the tangential direction [76]. The static and dynamic friction coefficients are respectively set to 0.2 and 0.1 in the model. The FE model of the specimen is shown in Fig. 3b.

Fig. 4 shows the results of FE model versus experiments for the concrete specimen under compressive load. The numerical results are provided for different values of $b_1$ parameter of Mat72_Rel3, which is the compressive damage scaling parameter. The objective of conducting the analysis for various values of $b_1$ was to extract the optimal value for $b_1$ ensuring the best alignment with experimental results. Based on Fig. 4, it is apparent that the compressive behaviour of concrete undergoes changes when the parameter $b_1$ is altered. However, it is difficult to say what value for $b_1$ parameter should be taken into account since there is a deviation between the numerical results and experiment for all examined $b_1$ values.

To enhance the compressive behaviour of concrete in this particular region, an investigation into the effect of η-λ function as damage curve is also taken into consideration. For this purpose, the effects of three distinct η-λ functions on the response behaviour have been investigated, by keeping constant the value of $b_1$ equal to −0.25. As already defined, the first curve is the auto-generated η-λ function (default η-λ function). The second η-λ function is adopted from Markovich et al. [29], and the third one is the proposed η-λ function in this paper. Essentially, an examination is being conducted on how the curvature of the concrete
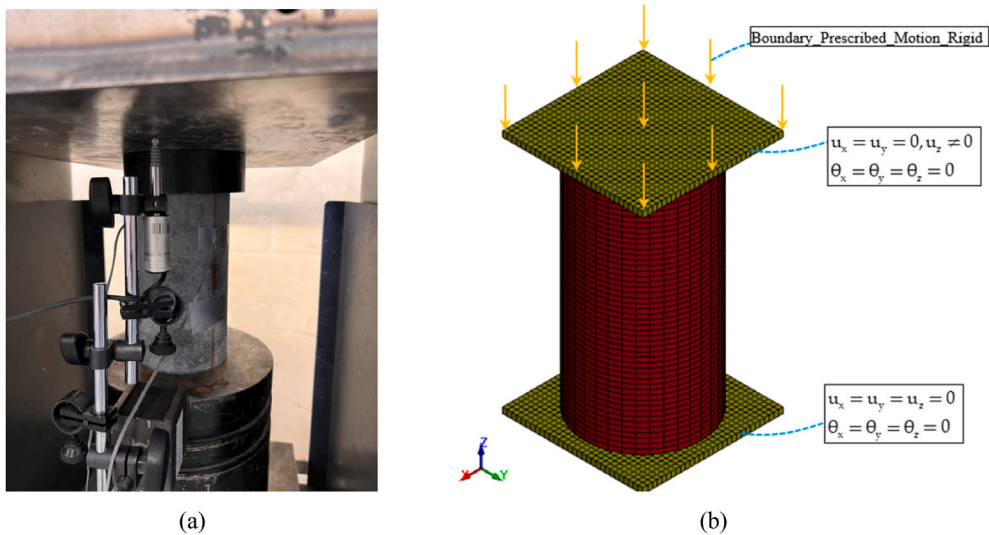
**Fig. 3.** Setup of compression test: (a) experiment, (b) Finite Element model.

compressive curve is influenced by these η-λ functions, with modifications occurring after the peak strength is reached. As shown in Fig. 5, the proposed η-λ function exhibits the highest level of compatibility with experimental data, in comparison to other damage functions, making it the preferred choice in the analyses presented in this study. Such a choice of η-λ function was derived based on trial-and-error simulations. It should be noted that the determination of damage parameters is typically grounded in the principle that energy dissipation per unit width equals the fracture energy of the material, often represented by the area enclosed by the stress-strain curve. This comparison between the strain-stress curves derived from finite element simulations and experimental data serves as a validation method. Previous research studies, exemplified by references such as [36,77], have adopted this strategy to define damage parameters. In practice, researchers employ a trial-and-error approach, experimenting with various values for these parameters to identify the optimal fit between numerical simulations and experimental results. For instance, in Refs. [78,79], a trial-and-error

procedure has been used to find the η-λ function, which in this study is also used to find the proposed η-λ function.

In the case of tensile behaviour, the method of single-element analysis has been used. This method is one of the most commonly employed techniques by researchers to calibrate proposed damage parameters of the material models with experimental data, particularly in the case of concrete materials. This technique, as illustrated in Fig. 6, is instrumental in assessing the impact of each parameter in material properties like Mat_72Rel3, on the results of numerical simulations under both tension and compression (with and without confining pressure from all four sides, see Fig. 6c. In this study, this method is only used for tensile behaviour since the stress-strain curve of a cubic specimen under the compressive load has not been recorded (instead, the cylindrical specimen was simulated under compressive axial load as discussed in the previous section). In this method, the applied loading is modelled using the prescribed boundary motion. Additionally, each node of the single element has its own boundary condition, as illustrated in Fig. 6. This
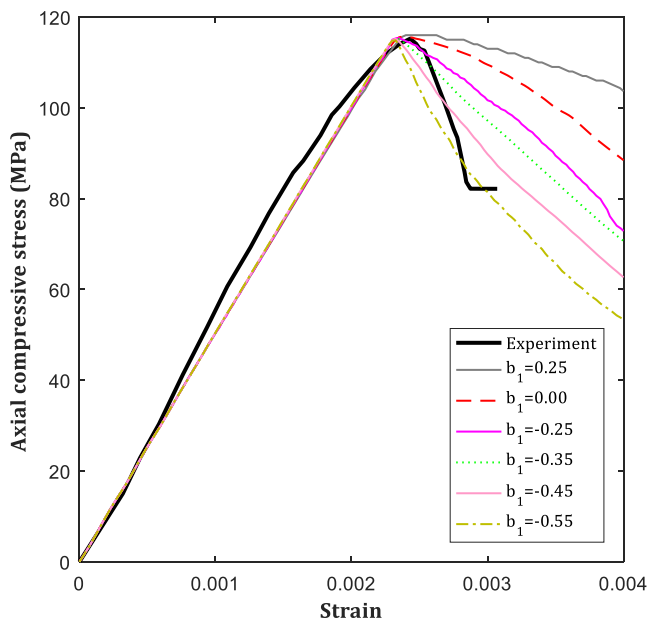


**Fig. 4.** Comparison of compressive stress-strain curve obtained from experiment and numerical modelling with different $b_1$ values.
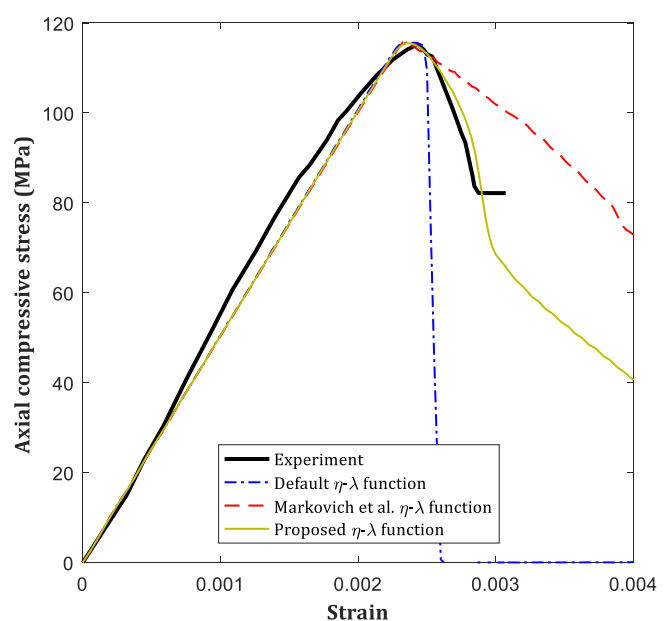


**Fig. 5.** Comparison of compressive stress-strain curve obtained from experiment and numerical modelling with different η-λ functions.
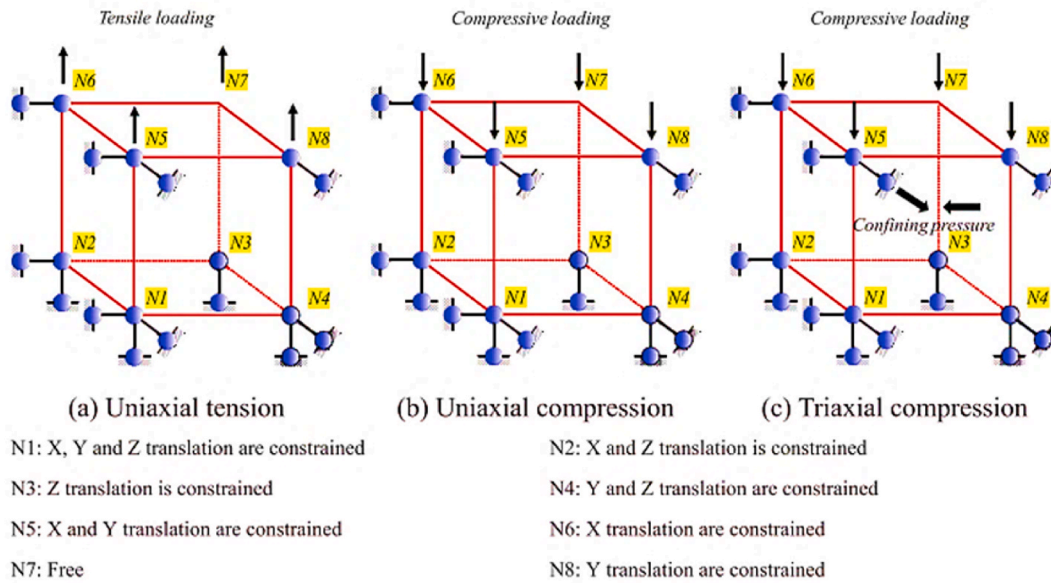
**Fig. 6.** Typical model setup of the single element model [20]: (a) uniaxial tension, (b) uniaxial compression, (c) triaxial compression.
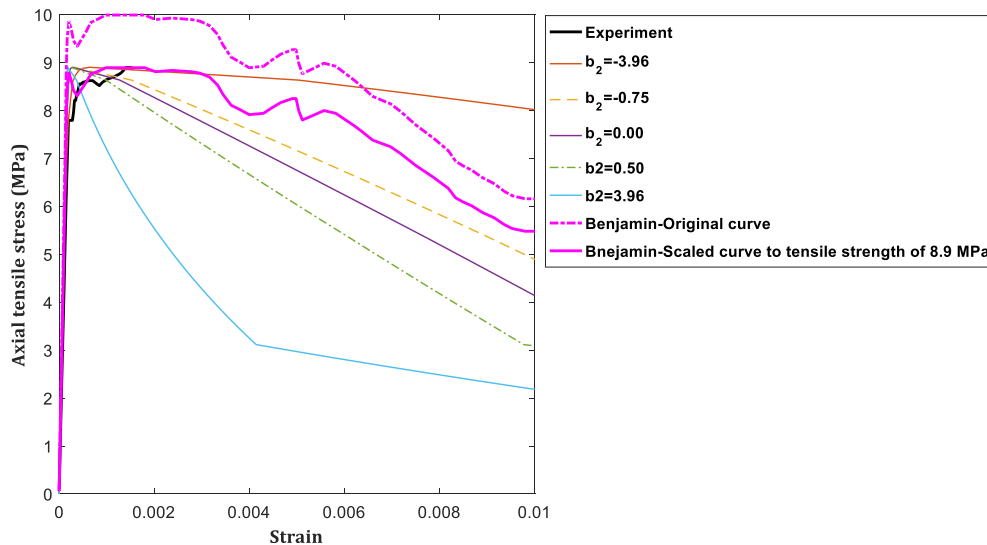


**Fig. 7.** Comparison of tensile stress-strain curve obtained from experiment and numerical modelling with different $b_2$ values.

approach is utilized to demonstrate the effectiveness of the material constitutive model in predicting the response of UHPFRC and, subsequently, to identify the optimal values for the parameters governing tension behaviour ($b_2$ value).

The numerical outcomes of the single element method are depicted in Fig. 7 for various $b_2$ values. As evident from the figure, the choice of $b_2$ value influences the results, and consequently, as can be seen, selecting $b_2 = -0.75$ can be considered in generating the stress-strain curve in the tensile region. It should be noted that the determination of the $b_2$ parameter is influenced by the behaviour of the sample after it reaches its peak tensile strength under tension. Limitations in equipment hindered the assessment of strains in UHPFRC beyond its peak tensile strength value in this study, necessitating an approximation for the tensile stress-strain behaviour of specimens up to higher strains. Leveraging the Benjamin curve from established technical literature (named as Benjamin Original Curve) [19,80] and scaling it to match the specimen's observed tensile strength of 8.9 MPa in this study (named as Benjamin Scaled curve), enabled an estimation of the post-peak tensile

behaviour of specimen (i.e., the specimen tested in this study) and into higher strains. As can be seen from Fig. 7, setting the $b_2$ parameter to $-0.75$ yielded a predicted curve closely resembling the scaled Benjamin Curve. However, the limitations of this study, particularly the lack of data collection for higher strain values in the tensile test, need to be declared. In other words, the adoption of the Benjamin Curve was resorted to, understanding that it provided a better estimation of the $b_2$ value. This approach, while acknowledging its inherent approximation, allowed for a rational estimation of the $b_2$ value, that can affect the results. It should be noted that, generally, by decreasing the $b_2$ parameter from a positive value to a negative value (like 3.96 to $-3.96$), the behaviour of the UHPFRC can be controlled, resulting in a more ductile specimen. In other words, by changing the value, more deflection can be interpreted, leading to an increase in the ductility of the specimen. Since fibre contents are used in UHPFRC, the specimens tend to have more ductility than normal concrete. Therefore, the $b_2$ parameter should be selected to balance the output, preventing the specimen from behaving very brittlely or in an overly ductile manner, which, by taking into
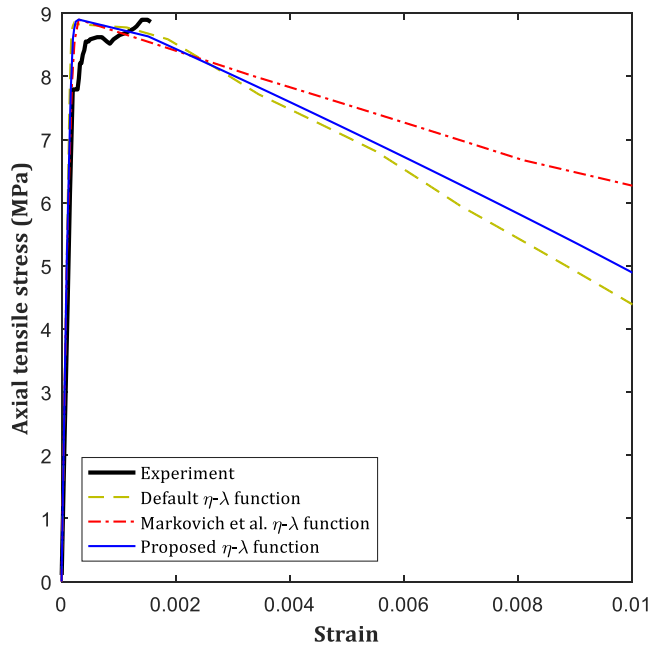
**Fig. 8.** Comparison of tensile stress-strain curve obtained from experiment and numerical modelling with different η-λ functions.

**Table 5**
EOS parameters and material properties of TNT and air.

| Material | Material model and EOS | Input parameters | Value |
|---|---|---|---|
| Air | MAT_NULL | Initial density, $\rho_0$ (g. mm$^{-3}$) | 1.29e-6 |
| | | Pressure cut-off | 0 |
| | EOS_LINEAR_POLYNOMIAL | $C_0$, $C_1$, $C_2$, $C_3$, $C_6$ | 0 |
| | | $C_4$, $C_5$ | 0.4 |
| | | Internal energy, $E_{0,air}$ (N/mm$^2$) | 0.25 |
| TNT | MAT_HIGH_EXPLOSIVE_BURN | Initial density, $\rho_0$ (g. mm$^{-3}$) | 1.63e-3 |
| | | Detonation velocity, $D$ (mm/msec) | 6930 |
| | | Chapman-Jouguet pressure, $P_{CJ}$ (MPa) | 21000 |
| | EOS_JWL | A (MPa) | 371200 |
| | | B (MPa) | 3231 |
| | | $R_1$ | 4.15 |
| | | $R_2$ | 0.95 |
| | | $\varsigma$ | 0.3 |
| | | Initial energy, $E_0$, TNT (N/mm$^2$) | 7000 |

account the effects of other damage parameters, the value of $-0.75$ for $b_2$ can be a good approximation in this study. In order to capture the effect of η-λ function on the tensile behaviour, a similar analysis that has already been done for compressive behaviour is also performed here with the same η-λ functions and keeping constant the value of $b_2$ equal to $-0.75$. The results from this investigation are shown in Fig. 8.

Overall, the results have elucidated the impact of parameters $b_1$, $b_2$, and η-λ function on the response of concrete subjected to both tensile and compressive loads. The refinement of concrete behaviour representation in both compressive and tensile regions, coupled with an increased number of experimental trials, holds the potential for more precise prediction and calibration of concrete parameters. In other words, it should be kept in mind that proposing a generic model that works for all types of UHPFRCs in both compression and tension is complicated and requires extensive experimentation and numerical modelling, which is beyond the scope of this study and this aspect will be subjected to further scrutiny and exploration in future investigations.

## 5. Blast load formulation and validation of FE modelling

### 5.1. Blast load formulation

To model blast loads, various strategies are available in the literature, which can be broadly categorized as simple and complex methods [81]. In the simple approach, the blast load is approximated as an exponential function of time and applied to the structure as a pressure history on the affected area [55]. The parameters for this idealized function can be determined using various empirical formulations found in the literature [82,83]. In contrast, the complex approach involves modelling TNT material and air as well as real conditions through the utilization of ALE (Arbitrary Lagrangian-Eulerian) in LS-DYNA [84,85]. This method often yields more accurate results (if all condition of experiment setup is known and available) compared to other blast loading approaches like Conwep, empirical formulations, pressure-impulse diagrams, etc. as simple approaches, but its computational cost is higher. Nevertheless, the simple strategies have also yielded promising outcomes, and many researchers have employed these methods with a reasonable degree of accuracy when compared to

experimental results. In this study, specifically within the part concerning the effect of blast loading, for a more comprehensive investigation of the issue, the two procedures including ALE method and load blast enhanced (LBE) method are utilized and the results are then compared together.

In case of ALE method, to model the air blast loading, both TNT and air are modelled using 3D finite elements. In this regard, the air is modelled as an ideal gas by using the MAT_NULL material model and the linear polynomial equation of state (i.e. EOS_LINEAR_POLYNOMIAL) is assigned, which gives the air pressure related to the volume and internal energy as follows:

$$P = C_0 + C_1\mu_a + C_2\mu_a{}^2 + C_3\mu_a{}^3 + (C_4 + C_5\mu_a + C_6\mu_a{}^2)E_{0,Air} \tag{9}$$

where $C_0$, $C_1$, $C_2$, $C_3$, $C_4$, $C_5$ and $C_6$ are the linear polynomial equation coefficients; $\mu_a = \rho/\rho_0 - 1$, in which $\rho$ and $\rho_0$ are the current and initial densities of air; and $E_{0,Air}$ is the internal energy per unit volume. The assigned values for these parameters are presented in Table 5.

To model TNT, the Mat_High_Explosive_Burn is used along with the Jones-Wilkins-Lee equation of state (i.e. EOS_JWL in LS-DYNA). The EOS_JWL defines denotation pressure as a function of the relative volume of the denotation product and an initial explosive internal energy, and it is expressed as follows:

$$P = A\left(1 - \frac{\omega}{R_1 V}\right)e^{-R_1 V} + B\left(1 - \frac{\omega}{R_2 V}\right)e^{-R_2 V} + \frac{\omega E_{0,TNT}}{V} \tag{10}$$

where $V$ is the relative volume of the detonation products; $A$, $B$, $R_1$, $R_2$, and $\omega$ are parameters related to the explosive type; and $E_{0,TNT}$ is the internal energy per unit volume (Table 5). It should be noted that for other input parameters, the default values are adopted.

Regarding the LBE method, it relies on the Kingery and Bulmash [86] relationships for free air blast generated by spherical and hemispherical surface charges of TNT. These air blast relationships align with those presented in UFC3-340-02 regulation [55] and the commonly referenced U.S. Army Engineer Research and Development Center (ERDC) application Conwep [87]. It should be noted that this method is applicable or restricted to scaled ranges greater than about 0.4 m/kg$^{1/3}$ [88].

### 5.2. Validation of FE modelling

In this section, to validate the accuracy of FE software in predicting the structural response under blast load, the previous experimental findings of Li et al. [17] have been used due to its utilization of a mixture design incorporating steel reinforcement, which, broadly speaking,
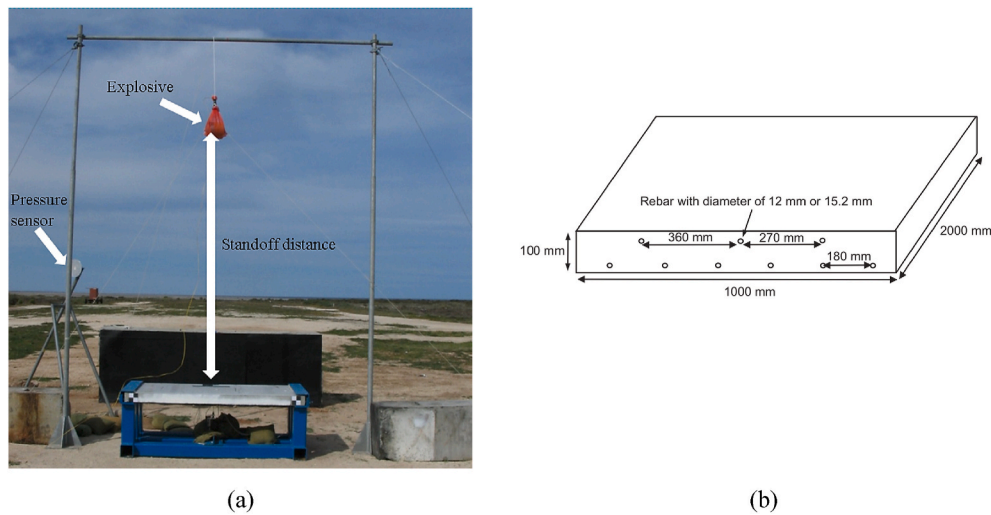
**Fig. 9.** Slab configuration and reinforcement; (a) experiment setup, (b) the schematic representation of UHPC slab and reinforcing rebars (the figures are adopted from Ref. [17]).

constitutes a fundamental aspect of UHPFRC material. The test specimens used for validation consisted of UHPC slabs with varying reinforcement ratios and different types of reinforcing steel, subjected to various blast scenarios with different explosive charge weights and stand-off distances. The field blast testing system and the schematic view of the UHPC panel are shown in Fig. 9a. The UHPC slabs (2000 mm × 1000 mm × 100 mm) were reinforced with steel rebars as depicted in Fig. 9b. No stirrup rebars were used in any of the panels. Regarding the material properties, the Young's modulus, Poisson's ratio, ultimate compressive strength, tensile strength, ultimate strain and density of UHPC specimens used in the experiments were set to 51503 MPa, 0.2, 128.9 MPa, 30 MPa, 0.0025 and 2424.9 kg/m$^3$, respectively. In the case of steel rebars, various steel strengths were employed in different specimens. It should be noted that no further details were provided on steel material except the yield stresses and rebar diameter, so the necessary information is derived from the existing literature on this type of material for the verification based on FE modelling.

More in detail, two experiments were employed in this paper for verification, denoted as Test 1 and Test 2 which correspond to the UHPC-D4 and UHPC-D3B tests performed by Li et al. [17], respectively. In Test 1, the explosive charge weight (W) and scaled distance (Z) were set to 8 kg of TNT and 0.5 m/kg$^{1/3}$, respectively. Utilizing equation Z = R/W$^{1/3}$, the stand-off distance (R), which is the distance between the explosive material and structure (here is the UHPC slab), was calculated as 1.0 m. Furthermore, Test 1 employed a steel ratio of 0.8 %, utilizing mild steel grade rebars with a diameter of 12 mm and a strength of 300 MPa. In Test 2, the explosive charge was increased to 14 kg of TNT, and the scaled blast distance was adjusted to 0.41, resulting in a stand-off distance of 1 m. The remaining parameters in Test 2, including the steel ratio, steel strength, and rebar diameter, were the same as those in Test 1. Li et al. [17] explored UHPC panels under blast loads using three different scaled distance values: 0.41, 0.50, and 3.05 m/kg$^{1/3}$. Notably, the blast scenario with Z = 3.05 m/kg$^{1/3}$ exhibited negligible impact on the panels and was consequently excluded from the validation process. In other words, Tests 1 and 2 significantly influenced the panel responses, leading to nonlinear behaviour. These tests are considered in the validation to assess the suitability of FE modelling in capturing post-yield behaviour of the panels.

In order to simulate the behaviour of UHPC slab under blast, the MM-ALE method was utilized, incorporating UHPC slab, steel rebars and supports (i.e. the experiment setup that held the UHPC slab during the test and provided the support conditions) as Lagrangian parts, and TNT and air parts as Eulerian parts. The coupling between ALE and Lagrangian parts has been taken into consideration by CONSTRAINED_LAGRANGE_IN_SOLID.

For modelling the UHPC slab, three-dimensional solid elements were employed, and the Mat72_Rel3 material model was used. Also, the EOS_TABULATED_COMPACTION is considered for equation of state of UHPC material, and its input parameters have been calculated by the method provided in Section 3. The strain rate effect is introduced in the modelling according to the formulation provided in Section 3.

The rebars were modelled using beam elements with the Hughes-Liu cross section integration method. The MAT_PLASTIC_KINEMATIC is utilized to consider the behaviour of steel material. The density, elastic modulus, Poisson ratio and yield stress of steel material are set to 7850 kg/m$^3$, 210000 MPa, 0.3, and 300 MPa. The strain rate effect is also considered by Cowper-Symmonds relationship with parameters C = 40.4 and P = 5.0, due to the fact that these values are reported for mild-steel in the literature [89–91], and it is assumed that it can be adopted for this case that there is no further information. It's important to highlight that, apart from the yield stress, the authors made assumptions regarding other parameters, as no additional details were provided in Li et al. [17]. To establish the contact between concrete and reinforcement bars in MM-ALE method, the ALE_COUPLING_NODAL_CONSTRAINT was employed.

For support conditions, solid elements were employed, and MAT_RIGID was utilized under the assumption that the support remains rigid and does not undergo deformation during the experiment. Due to the fact that the UHPC slab was placed on steel supports (Fig. 9a), their contact was taken into consideration with the CONTACT_AUTOMATIC_SURFACE_TO_SURFACE option.

The TNT and air parts were modelled using the method and formulation provided in Section 5, where details regarding material modelling, equation of state (EOS), and material properties were precisely described. Solid elements with ELFORM 11 of point ALE multi-material element are used for both TNT and air parts. In order to generate the three-dimensional mesh of TNT and Air parts, the Structured ALE has been employed.

The spacing parameters are input through the ALE_STRUCTURED_MESH_CONTROL_POINTS cards, from −1000 to +3000 mm in x-direction with 51 element number, from −1000 to +2000 mm in y-direction with 51 element number, and from −200 to +3000 mm in z-direction with 56 element number (about 140000 air elements). It should be noted that the local coordinate system is defined using the ALE_STRUCTURED_MESH by considering the previous values for element numbers and interval limits in x, y and z direction. The FE
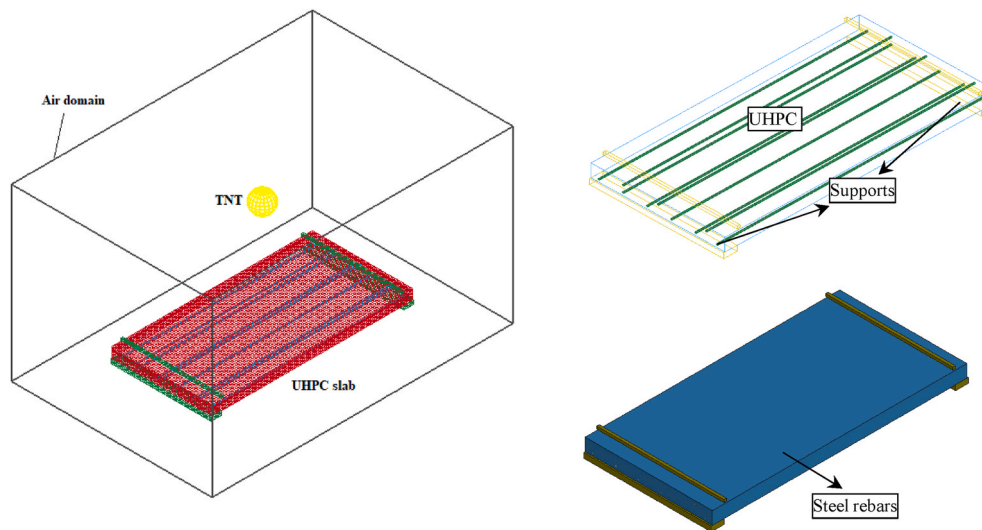
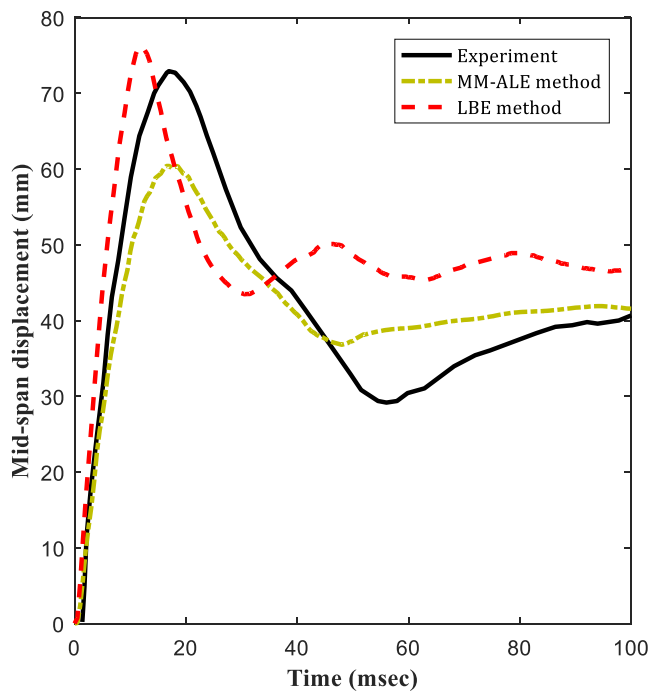**Fig. 10.** UHPC Slab configuration and reinforcement.



**Fig. 11.** Comparison the mid-span displacement time histories of the test slab obtained from MM-ALE method and load blast enhanced with the experiment results.

model and its details are shown in Fig. 10.

It is noteworthy that the "erosion" algorithm has been employed using the Mat_Add_Erosion to capture the initiation and propagation of concrete material damage. Careful consideration should be taken into account when it comes to setting the erosion criterion, since too high value may result in element distortion due to substantial deformation, while setting it too low may lead to premature erosion and element deletion, violating mass conservation and compromising result reliability. In this study, to prevent extensive removal of elements that would compromise mass conservation, a principal tensile strain value of 0.1 is employed as the erosion criterion [17]. For steel reinforcements, the value 0.2 is set for failure strain for eroding elements in MAT_-PLASTIC_KINEMATIC [92].

The time history of the out-of-plane mid-span displacement of UHPC panel for Test 1 is show in Fig. 11. According to the figure, the FE simulation based on MM-ALE method yields a maximum out-of-plane displacement of 60.43 mm at the midspan of the UHPC slab, exhibiting a deviation of 17.4 % in comparison to the 72.91 mm displacement observed in the experiments. Moreover, the residual mid-span deflection is calculated as 38.15 mm through numerical simulation, showing a deviation of 4.6 % when compared to the experimental value of 40 mm. In case of LBE method, a maximum displacement of 76.18 mm was obtained at the slab mid-span, showing a 4.3 % difference compared to the experimental maximum value of 72.91 mm. Additionally, the residual deflection induced in the slab was calculated as 43.4 mm, exhibiting a 7.8 % difference compared to the experimental value which was 40 mm. From the obtained results, it can be said that the ALE demonstrated a residual deflection calculation that closely matched experimental results. It is essential to noted that, in this experiment, the lack of certain laboratory specifications and the reliance on assumed input parameters by the authors might introduce disparities between the results of experimental and ALE method. Naturally, if the ALE method could encompass all experimental conditions, given its composite nature involving both Lagrangian and Eulerian approaches to capture blast wave interactions and propagation, the accuracy would notably improve. Conversely, the LBE method, with its simplicity and lower computational cost, has demonstrated acceptable accuracy and is recommended in scenarios demanding more extensive analyses, particularly when parametric analysis through repetitions is necessary. According to the study of Abedini et al. [93], for rapid analysis of a structure under blast load, the LBE method is more suitable than ALE method. However, if the simulation of the propagation of shock waves is needed, then ALE is the best approach. Since analysing the shock wave propagation of blast load is not the objective of this study, the LBE method has been used in section 6, with the aim of optimizing time efficiency and expediting other numerical analyses. It should be noted that, since the FE modelling has enough accuracy and efficiency in modelling the blast effect on structures, it can be implemented to other configurations with different geometry, material properties etc., which will be followed in the next sections.

Based on the experimental outcomes, the mid-span of the slab exhibits a predominant flexural mode due to the specific supports (two sides constrained only). As depicted in Fig. 12, the numerical model captures this behaviour in Test 1. In case of Test 2, the results shown in Fig. 13 indicate that the UHPC slab experienced failure, aligning precisely with the findings reported in Li et al. [17].
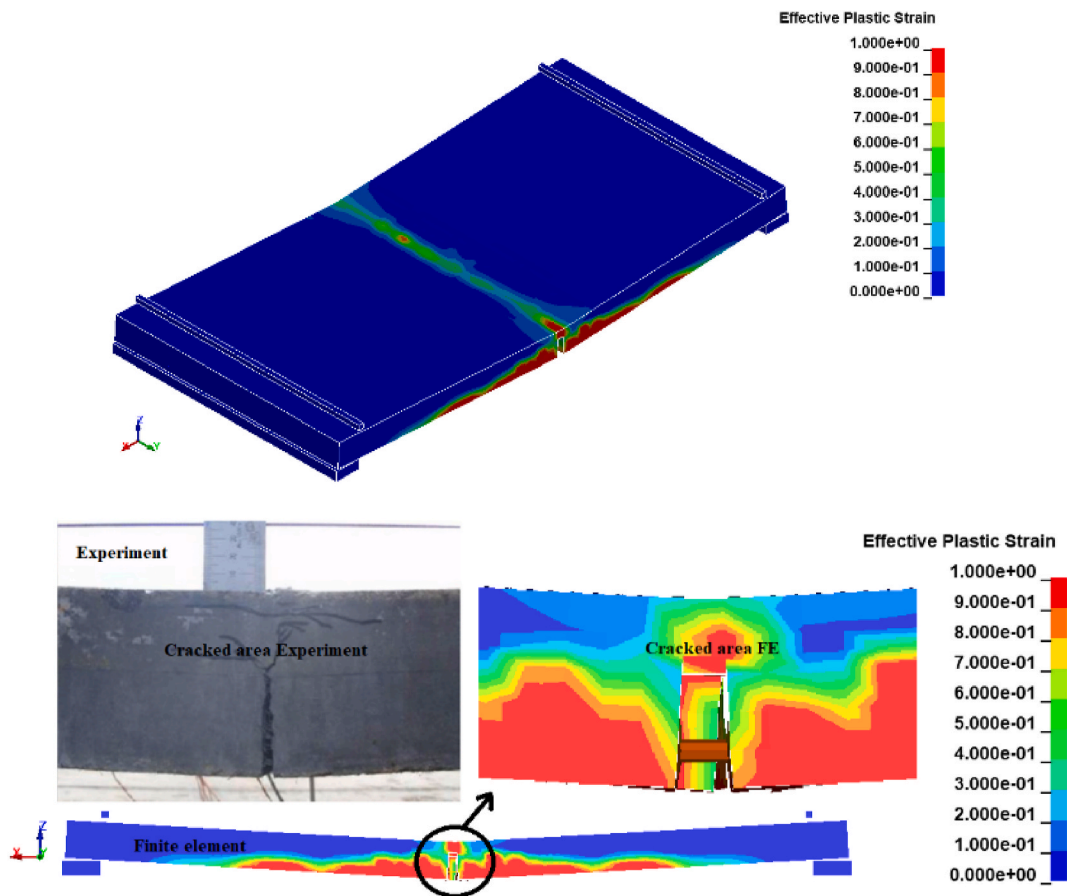
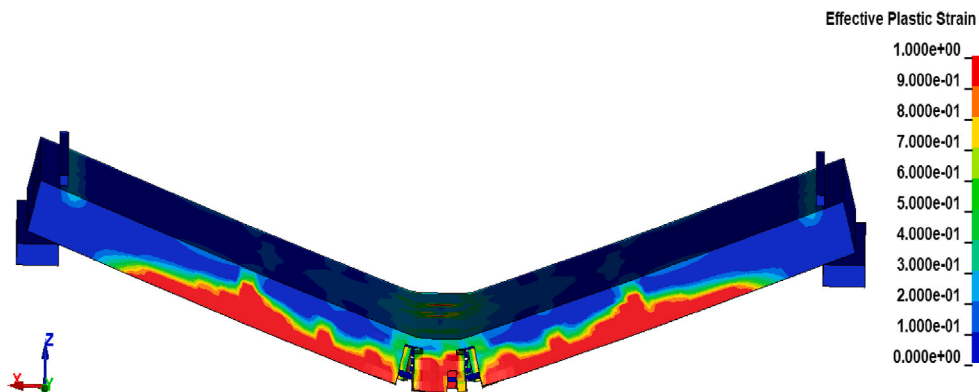**Fig. 12.** Comparison of results from the numerical model based on LS-DYNA software and Test 1.



**Fig. 13.** Comparison of results from the numerical model based on LS-DYNA software and Test 2.

## 6. Extending the FE model

Acknowledging that each structural element may exhibit support conditions ranging from hinge to fixed supports (excluding free ends), the calculations are performed under hinge support condition, which leads to larger deflections than fixed condition (this helps to find response for the case with high deflection that stands in case of more safety factor). Furthermore, building on the insights gained from the previous section, the LBE method is utilized for determining explosive forces due to its relatively commendable accuracy and less computational effort. It should be noted that finite element simulations have been performed by the Explicit solver of LS-DYNA, which avoids matrix evaluation and iteration, and thus, it is suitable for complex dynamic problems such as impacts and blasts. This is because LS-DYNA automatically evaluates the finite element mesh and material properties to determine an appropriate time step size for numerical stability. This time step size is then automatically adjusted throughout the transient analysis to account for contact, as well as local material and geometric nonlinearities [94,95].

### 6.1. Model configurations and blast scenarios

The FE model was further extended to perform a comprehensive examination of the optimized UHPFRC mixture (by taking into account its material properties in LS-DYNA through what was provided in sections 2 and 3) through the investigation of four distinct configurations under various blast loads. Four distinct configurations were examined, encompassing: 1) non-reinforced NSC panel (NR-NSC), 2) reinforced NSC panel (R–NSC), 3) non-reinforced UHPFRC panel (NR-UHPFRC), and 4) reinforced UHPFRC panel (R–UHPFRC). For all cases, the pinned condition has been applied to the panels. While various support conditions can be considered for the panel, it was assumed in this paper that the panel has pinned support conditions on all four sides. However, deformations and rotations are reduced by changing from hinged to fixed support conditions. In other words, these support conditions were chosen to achieve a safer design. The panel dimensions were set to 1.0 m by 1.0 m, with a thickness of 6.0 cm as $t_p$ (as will be discussed later, the simulations will also be extended to other thicknesses). It is worth mentioning that dimensions 1.0 m by 1.0 m were chosen based on practical considerations for on-site construction and transportation. Increased dimension would be required for larger thickness to prevent greater deflection under constant explosion forces, leading to increased weight and more difficult installation. Furthermore, in configurations 2 and 4 (to reinforce the panels), steel reinforcement bars were implemented (7 rebars in each direction – 14 in total – with 10 mm diameter and spaced at 150 mm), accompanied by a 20 mm concrete cover on both sides of the panel. It should be noted that due to practical constraints arising from the relatively low thickness of the examined panels (practical construction of these panels later on presents challenges), it is likely unfeasible or not practical to place two layers of rebar mesh on the bottom and top sides of the panel cross-section through a small thickness. Although adding extra layers of rebars is possible, only one layer of rebar mesh in the middle part of the panel (in which the rebars are oriented in perpendicular directions) was utilized in this study for

reinforced panels (this provides the same cover thickness at the top and bottom sides of the panels). The rebars were set in A2 type, boasting a yield stress of 340 MPa. The material properties of UHPFRC were considered as in Table 2, while the compressive strength and tensile strength of NSC were set to 30 MPa and 3.012 MPa, respectively. It should be noted that the strain rate effects of normal strength concrete were also taken into consideration, according to Refs. [96–98]. It should be noted that a mesh sensitivity analysis was conducted to determine optimal sizes for solid and beam elements, aiming to achieve both accuracy and computational efficiency in the analysis. The analysis encompassed different mesh dimensions, including 40 mm, 20 mm, 10 mm, and 5 mm. Results revealed that using solid elements with a maximum size of 10 mm, alongside beam elements of 10 mm length, yielded convergent outcomes with less than 1 % deviation compared to a finer mesh (5.0 mm). Mesh sizes of 20 mm and 40 mm exhibited deviations of 2.55 % and 15.5 %, respectively, compared to the 5 mm mesh, then the 10 mm mesh size was selected here to conduct simulations.

To select blast scenarios, recent incidents involving explosions have highlighted that terrorist attacks are commonly categorized based on two key factors: the weight of the explosive charge and the distance of detonation from the targeted structure. In documents like FEMA 426 [99] and FEMA 452 [100], the magnitude of explosions is classified by considering the amount of explosives that can be carried by individuals and various types of vehicles [101,102]. In this regard, various scenarios for explosive loading were taken into account to conduct numerical analyses which is shown in Table 6.

From FE analyses, the obtained maximum displacement ($\delta_{max}$) is presented in Table 6. The results reveal that, for all blast scenarios, the NR-NSC panels succumb to complete failure, undergoing extensive damage due to the applied blast loads. On the other hand, the R–NSC panels exhibit resilience, effectively absorbing explosion-induced loads only in scenarios 1 and 2, while succumbing to complete failure in the other scenarios (i.e., blast scenarios 3–6). Furthermore, the utilization of NR-UHPFRC panels, in contrast to their counterparts with NR-NSC and R–NSC panels, demonstrates superior performance. Notably, in blast scenarios 1 and 2, the maximum displacement recorded is significantly reduced. In blast scenario 3, the R–NSC panel experienced full failure, whereas the NR-UHPFRC panel successfully absorbed the explosion energy, achieving a maximum displacement of 11.07 mm. In the remaining blast scenarios (i.e., blast scenarios 4–6), the NR-UHPRFC panel undergoes damage, indicative of a substantial blast load intensity. However, when the UHPFRC material is reinforced with steel rebars, its overall behaviour witnesses a marked improvement, preventing complete failure in all cases. Nevertheless, it is noteworthy that the maximum member displacement remains considerably high in scenarios 5 and 6 for R–UHPFRC panels. The time histories of the mid-span displacement of panels for loading scenarios 1 and 2 are illustrated in Fig. 14a and b, respectively. It is important to note that, in order to effectively illustrate the distinctions among the results obtained for various cases, the horizontal axis (i.e., time) is restricted to 15 ms. For blast scenario 1, the maximum displacement of the NR-NSC panel which is 14.81 mm, almost occurred at 100 ms. However, in blast scenario 2, the NR-NSC panel experienced complete failure, with the displacement

**Table 6**
Selected blast scenarios for numerical modelling.

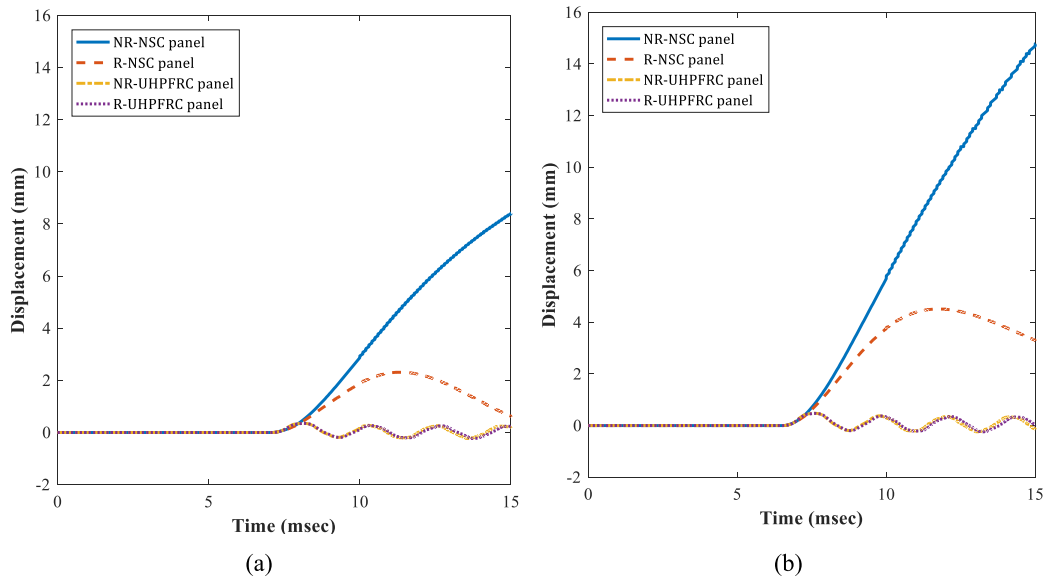| Blast scenarios | | | | $\delta_{max}$ (mm) | | | |
|---|---|---|---|---|---|---|---|
| Number of blast scenario | W (kg of TNT) | R (m) | Z (m/kg1/3) | NR-NSC | R–NSC | NR-UHPFRC | R–UHPFRC |
| 1 | 3.5 | 5.0 | 3.293 | 14.81 | 2.31 | 0.36 | 0.35 |
| 2 | 5.0 | 5.0 | 2.924 | Failure | 4.51 | 0.48 | 0.47 |
| 3 | 10.0 | 5.0 | 2.321 | Failure | 19.47 | 0.99 | 0.97 |
| 4 | 30.0 | 5.0 | 1.609 | Failure | Failure | 11.07 | 6.26 |
| 5 | 50.0 | 5.0 | 1.357 | Failure | Failure | Failure | 22.56 |
| 6 | 75.0 | 5.0 | 1.186 | Failure | Failure | Failure | 77.22 |

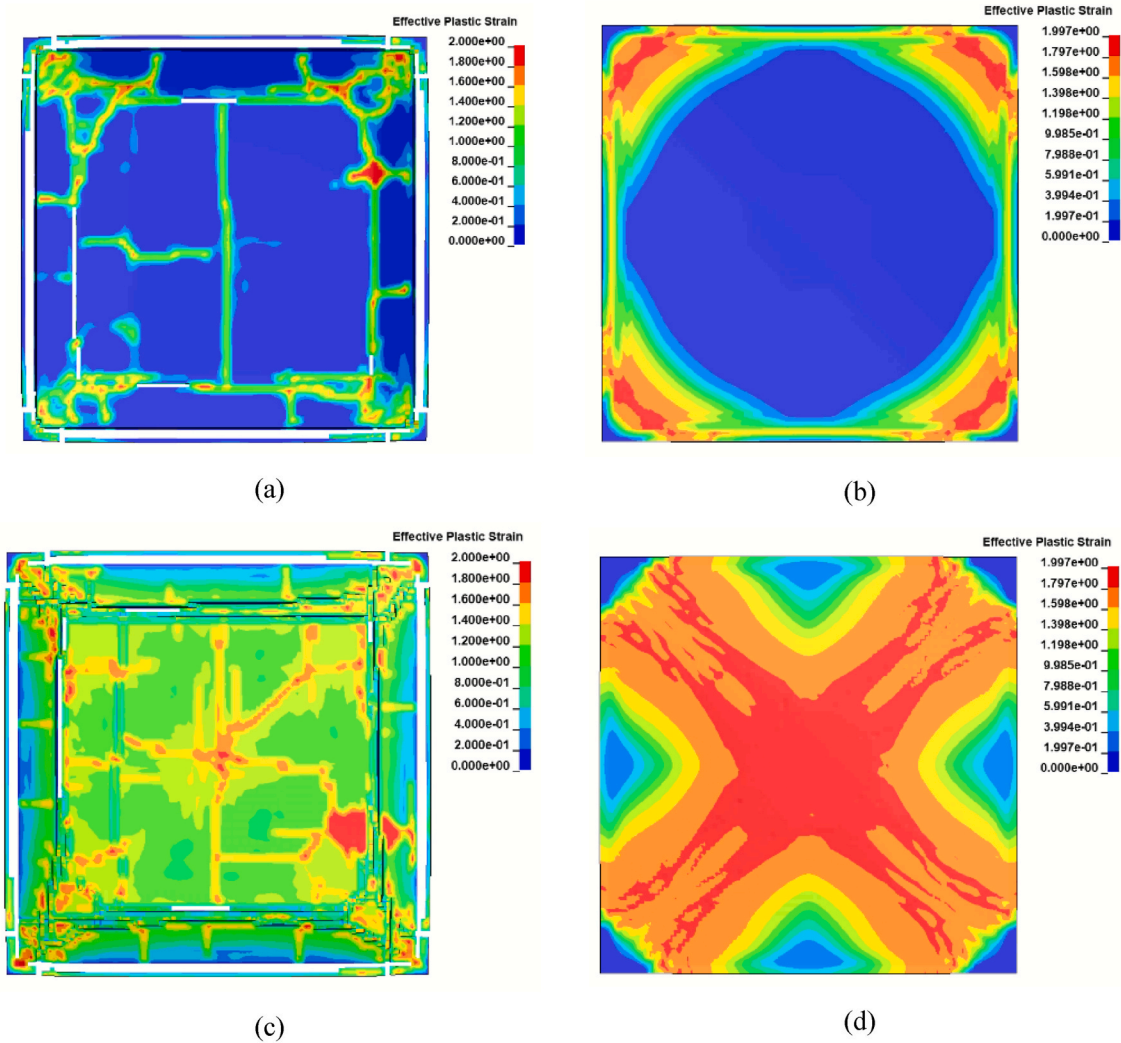**Fig. 14.** Time histories of maximum displacement for (a) blast scenario 1 and (b) blast scenario 2.



**Fig. 15.** Failure modes of the panel under W = 30 kg of TNT and R = 5.0 m; (a) front face of NR-NSC, (b) front face of NR-UHPFRC, (c) rear side of NR-NSC, (d) rear side of NR-UHPFRC.

reaching nearly 70 mm at 100 ms. In this case, the damage pattern was complete, with cracks propagating and the panel failing entirely. However, in both blast scenarios 1 and 2, the NR-UHPFRC and R–UHPFRC panels exhibit consistently elastic-linear behaviour. This underscores the exceptional overall performance of the proposed material, highlighting its remarkable capability to dissipate blast energy without incurring substantial damage. Notably, this resilience persists even when compared to cases where NR-NSC and R–NSC panels experience complete failure. These methodical investigations and parameter specifications contribute to a nuanced understanding of the structural response under varying conditions, essential for advancing the discourse in UHPFRC applications.

To further compare the obtained results, a comparison has been made on the damage pattern of the examined panels. Fig. 15 illustrates the damage caused to the NR-NSC and NR-UHPFRC panels, expressed in terms of effective plastic strain on both the front and rear faces of the panels, for the blast scenario 3 at time 8.20 ms. For the NR-NSC panel, the predominant failure mode is direct-shear failure. This failure mode is attributed to the shear stress near the support exceeding the concrete's shear strength, leading to the complete failure of this zone without any significant bending deformation. A key characteristic of direct-shear failure is the concentration of damage near the boundaries, as depicted in Fig. 15 (a) and Fig. 15 (c). Conversely, the NR-UHPFRC panel exhibits a flexural failure mode and damage is observed in the tensile zone at midspan (see Fig. 15 (d), with cracks propagating from the centre of the panel towards the supports. In the compressive zone on the front face of the panel which is shown in Fig. 15 (b), the effective plastic strain remains low, indicating minimal damage to the NR-UHPFRC material in this region. It is important to note that the failure modes of two-way panels are governed by direct-shear failure, flexural failure, or a combination of these mechanisms, known as flexural-shear failure. Each failure mode can occur depending on the energy released by the blast and can be investigated comprehensively. Furthermore, as investigated, for the same panel with NR-NSC or NR-UHPFRC, it is observed that using UHPFRC in comparison to NSC can significantly improve the behaviour of the panel and change its failure mode (e.g. from direct-shear failure to flexural failure), enhancing its overall structural behaviour under high strain conditions.

## 6.2. Minimum required thickness for the NR-UHPFRC panel

As demonstrated in the previous section, the NR-UHPFRC panels exhibit relatively good resistance to blast loads. It can effectively absorb a significant portion of explosion energy without undergoing extensive damage in comparison to NR-NSC and R–NSC panels. In this section, the focus is on determining the minimum required thickness for the panel using a damage index based on the support rotation criterion in such a way that the damage falls within the low range. To accomplish this objective, a brief explanation of the single support rotation criterion is first provided. In the structural design process for a structure or its individual members under blast loads, the conventional approach involves the consideration of performance-based design. In simpler terms, the acceptability of a selected member is determined by analysing its deformations in response to the applied blast load [55,103]. The anticipated support rotation $\theta$ is typically derived from the interplay between the maximum displacements ($\delta_{max}$) of the specific member and its length (L) and it is as follows:

$$\theta = tan^{-1}\left(\frac{\delta_{max}}{0.5L}\right) \qquad (11)$$

The estimated rotation amplitude shall then be compared with a set of limit values stipulated by standards, such as the provisions outlined in Refs. [55,103]. Although in these regulations various response limits are stipulated for reinforced concrete members (such as beams, columns, slabs, etc., taking into account different reinforcement conditions), the regulations do not provide specific guidelines for UHPRFC sections.

**Table 7**
Selected blast scenarios and examined standoff distance range for finding minimum required panel thickness.

| W (kg of TNT) | Range of R(m) (for $t_p = 40$ mm) | Range of R (m) (for $t_p = 60$ mm) | Range of R (m) (for $t_p = 80$ mm) | Range of R(m) (for $t_p = 100$ mm) |
|---|---|---|---|---|
| 3.5 | 2.2–4.0 | 1.5–2.5 | 1.1–2.0 | 0.9–1.5 |
| 10.0 | 3.9–7.0 | 2.7–4.5 | 2.1–3.5 | 1.7–3.0 |
| 30.0 | 6.7–10.0 | 4.8–8.0 | 3.7–6.0 | 3.1–5.0 |

Building on the findings from the previous section, it was demonstrated that the response of the NR-UHPFRC panel surpasses that of both NR-NSC and R–NSC panels. This implies that opting for the proposed allowable values intended for R–NSC when selecting them for the NR-UHPFRC panel would be a prudent choice to find the response of the structure. In Ref. [103], the allowable support rotation criterion ($\theta_a$) for reinforced beams, slabs and wall panels under blast load is proposed as 1, 2 and 5° for low, medium and high response, respectively. To ensure that minimal structural damage is incurred under blast loads, it is imperative that the support rotation be kept at fewer than $\theta_a = 1°$. To this aim, initially, for the determination of the minimum thickness, a standard geometry is considered (a panel with dimensions of 1 m by 1 m, where $t_p$ is the thickness). Due to the complexity of determining the initial required thickness at the first trial for a given blast load scenario, it is better to perform numerical studies based on a predefined thickness value and find the response of panel ($\theta$) under different blast scenarios which are outlined in Table 7 for different predefined thicknesses. For each geometry, the support rotation is obtained as a function of scaled distance. By fitting a curve to the obtained data, the scaled distance corresponding to a support rotation of 1° can be identified (which physically corresponds to the blast load which the panel behaves the rotation of 1° under its effect, and the limit value for the panel to have damage level below low damage). The obtained scaled distances of different configurations correspond to support rotation 1° are then used in establishing a relationship between minimum required thickness values, explosive charge weight and scaled distance. This relationship, once determined, becomes a practical tool for the determination of the required thickness for various blast scenarios, allowing for adaptability to changes in blast loads.

The results are presented in Fig. 16. It is evident that, in each curve, as the scaled distance decreases, there is an increase in support rotation, indicating a corresponding increase in damage for all cases. It should be noted that each of the derived figures for the panel maintains a consistent thickness. For instance, Fig. 16a is obtained for a panel with 40 mm thickness. For an equal scaled distance (2.0 m/kg$^{1/3}$), the results reveal that an escalation in explosive charge weight induces a proportional increase in the rotation of the support or, more precisely, amplifies the extent of damage inflicted upon the panel. The critical inference is that a similar scaled distance in explosion loading does not translate to a uniform explosion load when charge weight differs. This is consistent with the insights presented in technical literature. For example, in accordance with the Kingery-Bulmash relationships [86,91], explosion loading pressure is solely dependent on scaled distance. Conversely, blast time duration is not only a function of scaled distance but also hinges on the explosive weight. A higher explosive weight leads to a higher blast time duration, consequently intensifying the blast impact on the structure. Furthermore, elevating the thickness value allows for the application of lower values of scaled distance, signifying more robust resistance to stronger blast loads on the structure. This observed phenomenon is attributed to the governing mode of the structure bending in the selected configurations. Increasing the thickness results in a higher moment of inertia, contributing to enhanced structural resilience against the applied blast loads.

To further investigate the obtained results and in order to find the minimum required thickness related to $\theta_a = 1$, using MATLAB software,
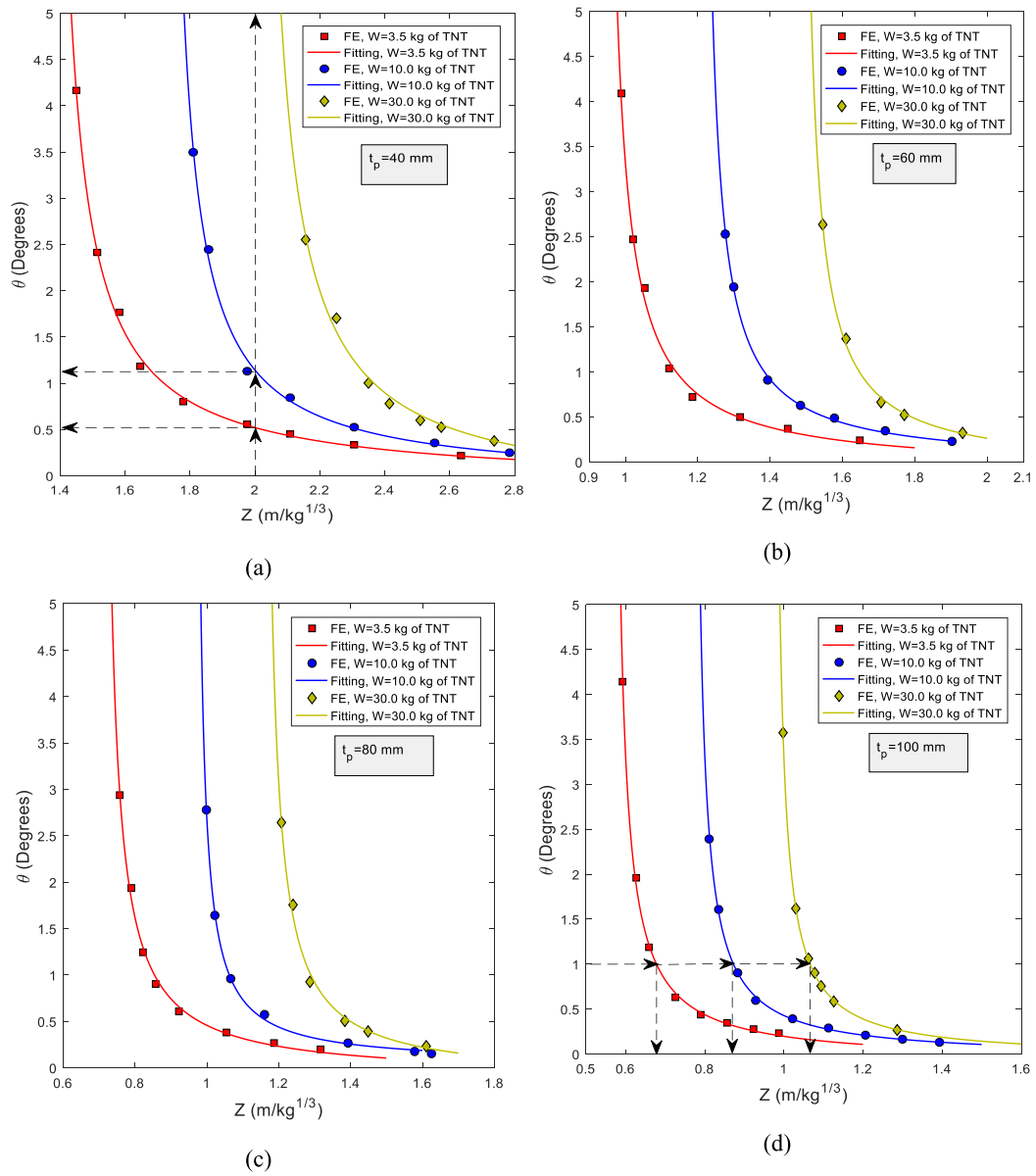
**Fig. 16.** Support rotation variation with scaled distance and charge weight for different panel thicknesses: (a) $t_p$ = 40 mm, (b) $t_p$ = 60 mm, (c) $t_p$ = 80 mm, (d) $t_p$ = 100 mm.

**Table 8**
Fitting coefficients.

| W (kg of TNT) | $t_p$ (mm) | $c_1$ | $c_2$ | $c_3$ | $R^2$ |
|---|---|---|---|---|---|
| 3.5 | 40 | −0.1012 | 2.492 | −3.377 | 0.998 |
| | 60 | −0.1073 | 4.354 | −4.063 | 0.996 |
| | 80 | −0.1038 | 6.003 | −4.221 | 0.994 |
| | 100 | −0.08848 | 8.022 | −4.519 | 0.999 |
| 10 | 40 | −0.07838 | 2.848 | −4.877 | 0.997 |
| | 60 | −0.03602 | 5.368 | −6.465 | 0.999 |
| | 80 | 0.03831 | 10.58 | −10.2 | 0.997 |
| | 100 | −0.04303 | 9.125 | −7.003 | 0.999 |
| 30 | 40 | −0.2553 | 2.117 | −4.214 | 0.991 |
| | 60 | −0.08969 | 5.423 | −8.012 | 0.998 |
| | 80 | −0.1233 | 6.464 | −7.443 | 0.996 |
| | 100 | −0.04738 | 9.919 | −9.62 | 0.999 |

a fitting curve was applied to each set of data obtained from FE components with the following equation.

$$\theta = c_1 + \frac{1}{c_2 \times Z + c_3} \tag{12}$$

where $c_1$, $c_2$ and $c_3$ are the fitting coefficients which are listed in Table 8 for each set of data and their relevant coefficient of determination $R^2$, which are higher than 0.99 in all cases, shows a very good accuracy in predicting the support rotation.

With the fitted functions, by setting the rotation equal to one and solving the equation in terms of scaled distance, the corresponding scaled distance value can be determined. This process is carried out for all cases, as schematically also illustrated in Fig. 16d, and the scaled distances related to $\theta_a = 1$ are obtained accordingly. It can be stated that each panel with a uniform thickness can withstand a certain level of scaled distance related to each examined explosive load. By obtaining these values and creating a database in terms of panel thickness, charge weight and scaled distance, a relationship can be proposed for thickness
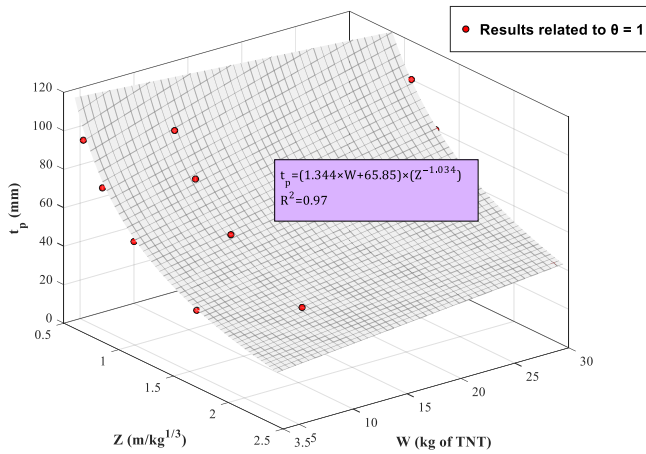
**Fig. 17.** Minimum required thickness of NR-UHPFRC panel as a function of W and Z.

as a function of charge weight and scaled distance. The proposed equation and fitted curve based on the obtained dataset with this procedure are shown in Fig. 17. As can be seen from the figure, the minimum required thickness of the panel can be calculated as a function of scaled distance and charge weight, which has a good level of accuracy with $R^2 = 0.97$.

In conclusion, to evaluate the applicability and potential of the analytical relationship presented in Fig. 17, two distinct examples were chosen to examine its efficacy in determining the minimum required thickness. The selected blast scenarios entailed W = 7.0 kg of TNT and R = 2.70 m for scenario 1, and W = 20.0 kg of TNT and R = 3.50 m for scenario 2. The analytical formulation yielded minimum required thickness values of 52.66 mm and 71.32 mm for scenarios 1 and 2, respectively. Subsequently, through simulations employing finite element modeling, it was observed that for the aforementioned selected scenarios, the minimum required thickness was 56.00 mm and 74.50 mm for scenarios 1 and 2, respectively (which are obtained by performing several simulations to find support rotation as 1°). These findings revealed disparities of 5.96 % and 4.23 % between the values derived from the analytical method and those from the finite element simulation. Nevertheless, despite these slight variations, a significant alignment between the results obtained by both methods was discerned, signifying the reliability and robustness of the analytical approach in estimating the minimum required thickness. It should be noted that the proposed formulation is derived based on the obtained data from the finite element simulations based on the selected geometry during the previous sections. For panels with different dimensions, different boundary conditions, etc. further investigation is needed.

### 6.3. Sensitivity analysis

Sensitivity analysis involves the modification of inputs or model parameters to assess the model's behaviour and understand the dependence of its outputs on these parameters [102,104,105]. In this section, a sensitivity analysis is conducted to examine how the response of UHPFRC panel responds to changes in input variables and identify the most and least influential parameters. In this process, one input variable is considered to be changed (New value = Origin value + 5 %, 10 %, 15 % and 20 %), while the values of all other parameters are kept constant (i.e., Origin value), and the resulting changes in the objective function ($\delta_{max}$) are measured. For this purpose, the NR-UHPFRC panel is considered with the same geometry, material properties and boundary condition reported in the previous section. The material properties selected as the origin values of the model for sensitivity analysis are based on the values proposed in Section 2. Furthermore, W = 20 kg of
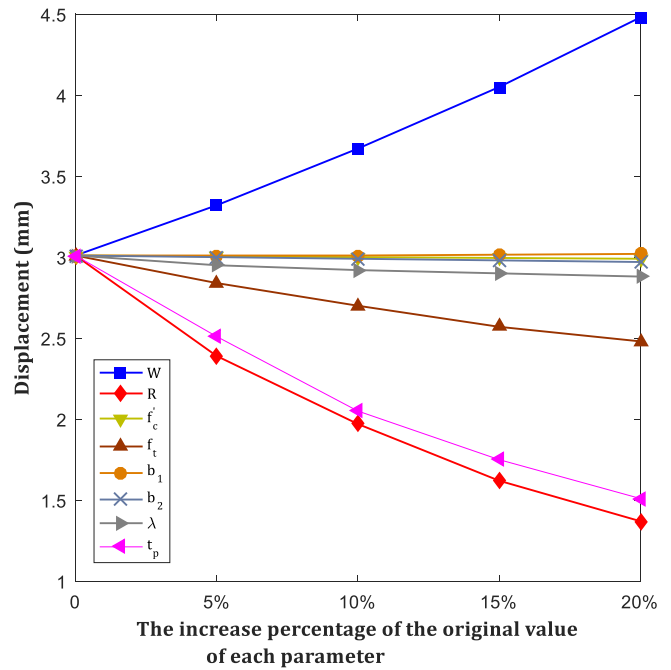


**Fig. 18.** Results of sensitivity analysis.

TNT and R = 5.0 m from the centre of the panel. The results are shown in Fig. 18.

Fig. 18 indicates that an increase in the explosive charge weight leads to an increase in the displacement of the panel, while an increase in the standoff distance results in a decrease in the displacement. Similarly, an increase in the panel thickness leads to a decrease in the displacement of the panel. Additionally, an increase in the tensile strength of concrete leads to a reduction in the panel displacement, and a similar behaviour is observed with an increase in the compressive strength of concrete. It is noteworthy that the sensitivity of the tensile strength parameter of the panel in this case is greater than the compressive strength of concrete. This is because, by maintaining a constant tensile strength and increasing compressive strength, concrete attains its ultimate tensile strength before reaching its ultimate compressive strength. Consequently, the panel's behaviour continues to be primarily governed by tension, rendering the increase in compressive strength perceived as inconsequential. Conversely, it is evident that an augmentation in tensile strength results in a reduction in the panel's displacement. This suggests that by increasing the tensile strength, the panel can withstand a higher level of stress in tension without entering the elastic region, leading to a decrease in displacement. In essence, the conclusion can be drawn that as long as concrete is predominantly controlled by tension, the impact of increasing compressive strength is less significant compared to enhancing tensile strength, and vice versa (for the NR-UHPFRC panel).

Another important point is that in this examined sensitivity analysis, failure parameters have had an impact on the structural response, with the greatest influence in this case coming from the parameter $\lambda$ in the $\eta$-$\lambda$ damage function. As mentioned earlier, the $\eta$-$\lambda$ damage function has a significant effect on the behaviour of the concrete panel and serves as a controller for the member's behaviour. Moreover, an increase in the parameter $b_1$ leads to a negligible increase in the panel's displacement.

On the other hand, an increase in the parameter $b_2$ has also resulted in a marginal reduction in displacement. This is because the original value of parameter $b_1$ was set at $-0.25$. During sensitivity analysis, when this value was multiplied by an incremental value (e.g., 1.2), it resulted in a reduction of the area enclosed by the stress-strain curve (or the fracture energy), consequently leading to an increase in panel displacement. Similarly, the initial value of parameter $b_2$ was $-0.75$.

During sensitivity analysis, when the original value was multiplied by an incremental value (e.g. 1.2), the area enclosed by the stress-strain curve in the tension region increased, leading to a decrease in the panel's displacement. The obtained results align with the observations from Figs. 4 and 7. It is worth noting that if the initial values of $b_1$ and $b_2$ are positive, increasing these parameters would result in a decrease and increase in the panel's displacement, respectively (Figs. 4 and 7).

In conclusion, it is evident that the most sensitive parameters are blast parameters and panel thickness. This gives a very important note that, if these parameters can be controlled in critical structures (for instance identifying and securing at-risk areas through preventive measures, particularly by installing secure barriers at an optimal distance from structures [56]), it is possible to prevent a significant extent of potential damages and minimize damage to primary structural elements and reduce the risk of progressive collapse.

## 7. Conclusions

This study delved into the dynamic response and damage investigation of blast-loaded Ultra-High Performance Fiber-Reinforced Concrete (UHPFRC) panels with optimized mixture design. Through a combination of experimental testing and advanced numerical analysis based on LS-DYNA software, valuable insights were gleaned into the effectiveness of UHPFRC in mitigating the effects of blast loading. The findings of this study are as follows.

- A calibrated and validated UHPFRC FE material model was achieved through meticulous adjustments of parameters based on experimental findings. The challenges associated with applying existing models to UHPFRC were revealed, emphasizing the necessity for recalibration to achieve optimal alignment between experimental and numerical results.
- A comprehensive numerical analysis was conducted utilizing LS-DYNA software, offering in-depth insights into the dynamic behaviour of UHPFRC panels under blast loading. Various model configurations and blast scenarios were covered, including non-reinforced normal strength concrete panel (NR-NSC), reinforced NSC panel (R–NSC), non-reinforced UHPFRC panel (NR-UHPFRC), and reinforced UHPFRC panel (R–UHPFRC). Results indicated that NR-NSC panels exhibited complete failure under blast loading, while R–NSC panels demonstrated resilience in specific scenarios. Notably, NR-UHPFRC panels outperformed their NSC and R–NSC counterparts, showcasing superior performance in absorbing explosion-induced loads. Furthermore, reinforcement with steel bars significantly enhanced the performance of R–UHPFRC panels, preventing complete failure in all considered blast scenarios. Also, for a same panel with NR-NSC or NR-UHPFRC, it is observed that using UHPFRC in comparison to NSC can significantly improve the behaviour of the panel and change its failure mode (e.g. from direct-shear failure to flexural failure), enhancing its overall structural behaviour under high strain conditions.
- The minimum required thickness for NR-UHPFRC panels using a proposed strategy based on a damage index derived from the support rotation criterion was determined in this study. Through numerical studies, a relationship between the minimum required thickness, explosive charge weight, and scaled distance was derived, emphasizing the crucial role of panel thickness in withstanding blast loads.
- The response of NR-UHPFRC panels to changes in input variables was assessed through a sensitivity analysis, with explosive charge weight, standoff distance, and panel thickness identified as dominant parameters. Valuable insights into the factors influencing the performance of UHPFRC panels under blast loading conditions were provided by this analysis, forming the basis for establishing the relationship between these parameters in this study.

## CRediT authorship contribution statement

**Mohammad Momeni:** Writing – original draft, Investigation, Formal analysis, Data curation. **Demetris Demetriou:** Writing – original draft, Formal analysis, Data curation. **Loucas Papadakis:** Writing – original draft, Supervision, Resources, Project administration, Investigation, Funding acquisition. **Chiara Bedon:** Writing – original draft, Investigation. **Michael F. Petrou:** Writing – original draft, Investigation, Formal analysis, Data curation. **Demetris Nicolaides:** Writing – original draft, Supervision, Resources, Project administration, Methodology, Funding acquisition, Conceptualization.

## Declaration of competing interest

The authors declare that they have no known competing financial interests or personal relationships that could have appeared to influence the work reported in this paper.

## Data availability

Data will be made available on request.

## Acknowledgments

## References

[1] A. Pai, C.R. Kini, S. Shenoy, Development of materials and structures for shielding applications against Blast and Ballistic impact: a Detailed Review, Thin-Walled Struct. 179 (2022) 109664.

[2] D. Nicolaides, A. Kanellopoulos, M. Petrou, P. Savva, A. Mina, Development of a new ultra high performance fibre reinforced cementitious composite (UHPFRCC) for impact and blast protection of structures, Construct. Build. Mater. 95 (2015) 667–674.

[3] R.S. Mijan, M. Momeni, M.A. Hadianfard, Impact of fine lightweight aggregates and coal waste on structural lightweight concrete: experimental study and gene expression programming, in: Proceedings of the Structures, 2024 106397.

[4] R. Al-Dala'ien, A. Syamsir, F. Usman, M. Abdullah, The effect of the W-shape stirrups shear reinforcement on the dynamic behavior of RC flat solid slab subjected to the low-velocity impact loading, Results in Engineering 19 (2023) 101353.

[5] S. Peyman, A. Eskandari, Analytical and numerical study of concrete slabs reinforced by steel rebars and perforated steel plates under blast loading, Results in Engineering 19 (2023) 101319.

[6] W. Mansour, S. Fayed, Flexural rigidity and ductility of RC beams reinforced with steel and recycled plastic fibers. Steel and Composite Structures, Int. J. 41 (2021) 317–334.

[7] D. Nicolaides, A. Kanellopoulos, P. Savva, A. Mina, M. Petrou, Mix design and mechanical properties of ultra high performance fibre reinforced cementitious composites (UHPFRCC), in: Proceedings of the Proceedings of the 1st International RILEM Conference on Rheology and Processing of Construction Materials, 2013. Paris, France.

[8] E. Madenci, S. Fayed, W. Mansour, Y.O. Özkılıç, Buckling performance of pultruded glass fiber reinforced polymer profiles infilled with waste steel fiber reinforced concrete under axial compression, Steel and Composite Structures, An International Journal 45 (2022) 653–663.

[9] D.-Y. Yoo, N. Banthia, Mechanical properties of ultra-high-performance fiber-reinforced concrete: a review, Cement Concr. Compos. 73 (2016) 267–280.

[10] Y. Shen, Y. Wang, S. Du, Z. Yang, H. Cheng, F. Wang, Effects of the adhesive layer on the multi-hit ballistic performance of ceramic/metal composite armors, J. Mater. Res. Technol. 13 (2021) 1496–1508.

[11] S. McCallum, The influence of preload and boundary conditions on pre-damaged composite plates subject to soft-body impact, Mater. Des. 83 (2015) 848–857.

[12] J. Xu, C. Wu, H. Xiang, Y. Su, Z.-X. Li, Q. Fang, H. Hao, Z. Liu, Y. Zhang, J. Li, Behaviour of ultra high performance fibre reinforced concrete columns subjected to blast loading, Eng. Struct. 118 (2016) 97–107.

[13] Q. Liao, J. Yu, X. Xie, J. Ye, F. Jiang, Experimental study of reinforced UHDC-UHPC panels under close-in blast loading, J. Build. Eng. 46 (2022) 103498.

[14] D. Nicolaides, A. Kanellopoulos, P. Savva, M. Petrou, Experimental field investigation of impact and blast load resistance of ultra high performance fibre reinforced cementitious composites (UHPFRCCs), Construct. Build. Mater. 95 (2015) 566–574.

[15] G.H. Mahmud, A.M. Hassan, S.W. Jones, G.K. Schleyer, Experimental and numerical studies of ultra high performance fibre reinforced concrete (UHPFRC) two-way slabs, in: Proceedings of the Structures, 2021, pp. 1763–1778.

[16] J.O. Hallquist, LS-DYNA Keyword User's Manual, vol. 970, Livermore Software Technology Corporation, 2007.

[17] J. Li, C. Wu, H. Hao, An experimental and numerical study of reinforced ultra-high performance concrete slabs under blast loads, Mater. Des. 82 (2015) 64–76.

[18] L. Mao, S. Barnett, D. Begg, G. Schleyer, G. Wight, Numerical simulation of ultra high performance fibre reinforced concrete panel subjected to blast loading, Int. J. Impact Eng. 64 (2014) 91–100.

[19] S. Xu, P. Wu, C. Wu, Calibration of KCC concrete model for UHPC against low-velocity impact, Int. J. Impact Eng. 144 (2020) 103648.

[20] Q. Su, H. Wu, Q. Fang, Calibration of KCC model for UHPC under impact and blast loadings, Cement Concr. Compos. 127 (2022) 104401.

[21] J.M. Magallanes, Importance of concrete material characterization and modelling to predicting the response of structures to shock and impact loading, Structures under shock and impact X 98 (2008) 241–250.

[22] Y. Wu, J.E. Crawford, J.M. Magallanes, Performance of LS-DYNA concrete constitutive models, in: Proceedings of the 12th International LS-DYNA Users Conference, 2012, pp. 1–14.

[23] Q. Wang, Q. Li, X. Yin, S. Xu, Z. Su, H. Xie, Fracture behavior and size effect of UHPFRC: experimental and meso-scale numerical investigation, Eng. Fract. Mech. 283 (2023) 109197.

[24] F. Zhou, Q. Su, Y. Cheng, P. Jia, H. Wu, Novel constitutive model of UHPC under impact and blast loadings considering compaction of shear dilation, Int. J. Impact Eng. 173 (2023) 104468.

[25] D. Saini, K. Oppong, B. Shafei, Investigation of concrete constitutive models for ultra-high performance fiber-reinforced concrete under low-velocity impact, Int. J. Impact Eng. 157 (2021) 103969.

[26] F. Zhang, A.S. Shedbale, R. Zhong, L.H. Poh, M.-H. Zhang, Ultra-high performance concrete subjected to high-velocity projectile impact: implementation of K&C model with consideration of failure surfaces and dynamic increase factors, Int. J. Impact Eng. 155 (2021) 103907.

[27] W. Guo, W. Fan, X. Shao, D. Shen, B. Chen, Constitutive model of ultra-high-performance fiber-reinforced concrete for low-velocity impact simulations, Compos. Struct. 185 (2018) 307–326.

[28] Y. Cao, Q. Yu, W. Tang, H. Brouwers, Numerical investigation on ballistic performance of coarse-aggregated layered UHPFRC, Construct. Build. Mater. 250 (2020) 118867.

[29] N. Markovich, E. Kochavi, G. Ben-Dor, An improved calibration of the concrete damage model, Finite Elem. Anal. Des. 47 (2011) 1280–1290.

[30] S. Xu, B. Chen, Q. Li, F. Zhou, X. Yin, X. Jiang, P. Wu, Experimental and numerical investigations on ultra-high toughness cementitious composite slabs subjected to close-in blast loadings, Cement Concr. Compos. 126 (2022) 104339.

[31] S. Xu, P. Yuan, J. Liu, X. Yu, Y. Hao, F. Hu, Y. Su, Experimental and numerical investigation of G-UHPC based novel multi-layer protective slabs under contact explosions, Eng. Fail. Anal. 142 (2022) 106830.

[32] P. Jia, H. Wu, Q. Fang, Q. Peng, L. Ma, TDOF model for UHPC members under lateral low-velocity impact, Int. J. Impact Eng. 174 (2023) 104520.

[33] D.K. Thai, S.E. Kim, Failure analysis of UHPFRC panels subjected to aircraft engine model impact, Eng. Fail. Anal. 57 (2015) 88–104.

[34] D.-K. Thai, S.-E. Kim, Prediction of UHPFRC panels thickness subjected to aircraft engine impact, Case Studies in Structural Engineering 5 (2016) 38–53.

[35] Y. Liu, J. Yang, G. Xu, H. Wei, E. Deng, Performance of UHPC bridge piers subjected to heavy vehicle collisions and probability analysis of damage level, in: Proceedings of the Structures, 2023, pp. 212–232.

[36] X. Lin, Numerical simulation of blast responses of ultra-high performance fibre reinforced concrete panels with strain-rate effect, Construct. Build. Mater. 176 (2018) 371–382.

[37] J. Wei, J. Li, C. Wu, H. Hao, J. Liu, Experimental and numerical study on the impact resistance of ultra-high performance concrete strengthened RC beams, Eng. Struct. 277 (2023) 115474.

[38] G. Gholipour, A.M. Billah, Dynamic behavior of bridge columns reinforced with shape memory alloy rebar and UHPFRC under lateral impact loads, Int. J. Impact Eng. 168 (2022) 104297.

[39] P. Jia, H. Wu, R. Wang, Q. Fang, Dynamic responses of reinforced ultra-high performance concrete members under low-velocity lateral impact, Int. J. Impact Eng. 150 (2021) 103818.

[40] W. Wang, C. Wu, J. Li, Z. Liu, Y. Lv, Behavior of ultra-high performance fiber-reinforced concrete (UHPFRC) filled steel tubular members under lateral impact loading, Int. J. Impact Eng. 132 (2019) 103314.

[41] H. Aoude, F.P. Dagenais, R.P. Burrell, M. Saatcioglu, Behavior of ultra-high performance fiber reinforced concrete columns under blast loading, Int. J. Impact Eng. 80 (2015) 185–202.

[42] G. Gholipour, A.M. Billah, Numerical investigation on the dynamic behavior of UHPFRC strengthened rocking concrete bridge piers subjected to vehicle collision, Eng. Struct. 288 (2023) 116241.

[43] W. Fan, R. Xie, M. Davidson, H. Yin, K. Lai, Q. Wu, Crashworthiness and energy absorption of UHPFRC-steel composite sandwich structures under impact loading, Compos. Struct. 311 (2023) 116813.

[44] T. Yang, W. Wang, Z. Liu, C. Wu, S. Xu, Y. Yang, Behavior of CFRP-UHPFRC-steel double skin tubular columns against low-velocity impact, Compos. Struct. 261 (2021) 113284.

[45] C. Li, H. Aoude, Behaviour of UHPFRC-retrofitted RC beams with varying strengthening configurations under single and repeated blast loading, Cement Concr. Compos. 142 (2023) 105180.

[46] S. Mirassi, M. Momeni, A. Hosseini Moorderaz, Damage evaluation of concrete bridge with steel piers subjected to explosive loads, Journal of Modeling in Engineering (2024).

[47] M. Momeni, C. Bedon, M.A. Hadianfard, Probabilistic evaluation of steel column damage under blast loading via simulation reliability methods and gene expression programming, Engineering Proceedings 53 (2023) 20.

[48] R. Hu, Z. Fang, C. Shi, B. Benmokrane, J. Su, A review on seismic behavior of ultra-high performance concrete members, Adv. Struct. Eng. 24 (2021) 1054–1069.

[49] N. Naeimi, M.A. Moustafa, Numerical modeling and design sensitivity of structural and seismic behavior of UHPC bridge piers, Eng. Struct. 219 (2020) 110792.

[50] J. Fládr, P. Bílý, J. Vodička, Experimental testing of resistance of ultra-high performance concrete to environmental loads, Procedia Eng. 151 (2016) 170–176.

[51] Y. Zhu, H. Hussein, A. Kumar, G. Chen, A review: material and structural properties of UHPC at elevated temperatures or fire conditions, Cement Concr. Compos. 123 (2021) 104212.

[52] H. Qin, J. Yang, K. Yan, J.-H. Doh, K. Wang, X. Zhang, Experimental research on the spalling behaviour of ultra-high performance concrete under fire conditions, Construct. Build. Mater. 303 (2021) 124464.

[53] S. Yang, X. Kong, H. Wu, Q. Fang, H. Xiang, Constitutive modelling of UHPCC material under impact and blast loadings, Int. J. Impact Eng. 153 (2021) 103860.

[54] X. Lin, Y. Zhang, P.J. Hazell, Modelling the response of reinforced concrete panels under blast loading, Mater. Des. 56 (2014) 620–628, 1980-2015.

[55] U. DoD, Structures to Resist the Effects of Accidental Explosions, US DoD, Washington, DC, USA, 2008.

[56] M. Momeni, C. Bedon, M.A. Hadianfard, A. Baghlani, An efficient reliability-based approach for evaluating safe scaled distance of steel columns under dynamic blast loads, Buildings 11 (2021) 606.

[57] C. Wu, H. Hao, Safe scaled distance for masonry infilled RC frame structures subjected to airblast loads, J. Perform. Constr. Facil. 21 (2007) 422–431.

[58] J. Feng, W. Li, C. Ding, D. Gao, Z. Shi, J. Liang, Numerical and analytical investigations on projectile perforation on steel–concrete–steel sandwich panels, Results in Engineering 8 (2020) 100164.

[59] J. Bruhl, W. Johnson, A. Varma, Design of SC Composite Walls for Projectile Impact: Local Failure, 2013.

[60] D.-K. Thai, S.-E. Kim, T.Q. Bui, Modified empirical formulas for predicting the thickness of RC panels under impact loading, Construct. Build. Mater. 169 (2018) 261–275.

[61] B. Pu, X. Wang, W. Li, J. Feng, Analytical model formulation of steel plate reinforced concrete walls against hard projectile impact, Appl. Sci. 12 (2022) 518.

[62] Q. Li, D. Tong, Perforation thickness and ballistic limit of concrete target subjected to rigid projectile impact, J. Eng. Mech. 129 (2003) 1083–1091.

[63] M. Alkaysi, S. El-Tawil, Z. Liu, W. Hansen, Effects of silica powder and cement type on durability of ultra high performance concrete (UHPC), Cement Concr. Compos. 66 (2016) 47–56.

[64] R.S. Rashid, S.M. Salem, N. Azreen, Y. Voo, M. Haniza, A. Shukri, M.-S. Yahya, Effect of elevated temperature to radiation shielding of ultra-high performance concrete with silica sand or magnetite, Construct. Build. Mater. 262 (2020) 120567.

[65] N. Van Tuan, G. Ye, K. Van Breugel, O. Copuroglu, Hydration and microstructure of ultra high performance concrete incorporating rice husk ash, Cement Concr. Res. 41 (2011) 1104–1111.

[66] S.-T. Kang, J.-I. Choi, K.-T. Koh, K.S. Lee, B.Y. Lee, Hybrid effects of steel fiber and microfiber on the tensile behavior of ultra-high performance concrete, Compos. Struct. 145 (2016) 37–42.

[67] D.-Y. Yoo, N. Banthia, Y.-S. Yoon, Flexural behavior of ultra-high-performance fiber-reinforced concrete beams reinforced with GFRP and steel rebars, Eng. Struct. 111 (2016) 246–262.

[68] H. Zhang, T. Ji, X. Zeng, Z. Yang, X. Lin, Y. Liang, Mechanical behavior of ultra-high performance concrete (UHPC) using recycled fine aggregate cured under different conditions and the mechanism based on integrated microstructural parameters, Construct. Build. Mater. 192 (2018) 489–507.

[69] L.F. Maya Duque, B. Graybeal, Fiber orientation distribution and tensile mechanical response in UHPFRC, Mater. Struct. 50 (2017) 1–17.

[70] D. Demetriou, T. Polydorou, K. Oikonomopoulou, P. Savva, I. Giannopoulou, P. M. Robert, O. Tsiolou, A. Lampropoulos, D. Nicolaides, M.F. Petrou, Optimising ultra-high-performance fiber-reinforced concrete for impact resistance, in: Proceedings of the International Symposium of the International Federation for Structural Concrete, 2023, pp. 967–976.

[71] Z. Tu, Y. Lu, Evaluation of typical concrete material models used in hydrocodes for high dynamic response simulations, Int. J. Impact Eng. 36 (2009) 132–146.

[72] X. Shilang, W. Ping, L. Qinghua, Z. Fei, L. Rui, Determination of K&C model parameters for ultra-high toughness cementitious composites, J. Build. Struct. 43 (2022) 233.

[73] J. Li, Y. Zhang, Evolution and calibration of a numerical model for modelling of hybrid-fibre ECC panels under high-velocity impact, Compos. Struct. 93 (2011) 2714–2722.

[74] W. Wang, D. Zhang, F. Lu, S.-c. Wang, F. Tang, Experimental study and numerical simulation of the damage mode of a square reinforced concrete slab under close-in explosion, Eng. Fail. Anal. 27 (2013) 41–51.

[75] B. Graybeal, Material property characterization of ultra-high performance concrete, FHWA (2006). Virginia; USA, Technical report, No. FHWA-HRT-06-103.

[76] J.O. Hallquist, LS-DYNA Keyword User's Manual, vol. 970, Livermore Software Technology Corporation, 2007, pp. 1–2.

[77] X. Lin, R.J. Gravina, An effective numerical model for reinforced concrete beams strengthened with high performance fibre reinforced cementitious composites, Mater. Struct. 50 (2017) 1–13.

[78] X. Yin, Q. Li, B. Chen, S. Xu, An improved calibration of Karagozian & Case concrete/cementitious model for strain-hardening fibre-reinforced cementitious composites under explosion and penetration loadings, Cement Concr. Compos. 137 (2023) 104911.

[79] C. Chen, X. Zhang, H. Hao, J. Cui, Discussion on the suitability of dynamic constitutive models for prediction of geopolymer concrete structural responses under blast and impact loading, Int. J. Impact Eng. 160 (2022) 104064.

[80] Z.B. Haber, I. De la Varga, B.A. Graybeal, B. Nakashoji, R. El-Helou, Properties and behavior of UHPC-class materials; United States, Federal Highway Administration. Office of Infrastructure … (2018).

[81] P. Shirbhate, M. Goel, A critical review of blast wave parameters and approaches for blast load mitigation, Arch. Comput. Methods Eng. 28 (2021) 1713–1730.

[82] A. Ullah, F. Ahmad, H.-W. Jang, S.-W. Kim, J.-W. Hong, Review of analytical and empirical estimations for incident blast pressure, KSCE J. Civ. Eng. 21 (2017) 2211–2225.

[83] T. Ngo, P. Mendis, A. Gupta, J. Ramsay, Blast loading and blast effects on structures–an overview, Electron. J. Struct. Eng. (2007) 76–91.

[84] S. Hyung-Cheol, Application of arbitrary Lagrangian-eulerian technique for air explosion structural analysis for naval ships using LS-DYNA, Journal of Ship and Ocean Technology 9 (2005) 38–46.

[85] M. Abedini, A.A. Mutalib, S.N. Raman, E. Akhlaghi, Modeling the effects of high strain rate loading on RC columns using Arbitrary Lagrangian Eulerian (ALE) technique, Rev. Int. Métodos Numéricos Cálculo Diseño Ing. 34 (2018).

[86] C.N. Kingery, G. Bulmash, Airblast Parameters from TNT Spherical Air Burst and Hemispherical Surface Burst; US Army Armament and Development Center, Ballistic Research Laboratory, 1984.

[87] D. Hyde, CONWEP: Conventional Weapons Effects Program, vol. 2, US Army Engineer Waterways Experiment Station, USA, 1991.

[88] L. Schwer, H. Teng, M. Souli, LS-DYNA air blast techniques: comparisons with experiments for close-in charges, in: Proceedings of the 10th European LS-DYNA Conference, 2015, pp. 15–17.

[89] G.R. Cowper, P.S. Symonds, Strain-hardening and Strain-Rate Effects in the Impact Loading of Cantilever Beams, Brown Univ Providence Ri, 1957.

[90] N. Jones, Structural Impact, Cambridge university press, 2011.

[91] M. Momeni, M.A. Hadianfard, C. Bedon, A. Baghlani, Numerical damage evaluation assessment of blast loaded steel columns with similar section properties, Structures 20 (2019) 189–203.

[92] M. Momeni, M.A. Hadianfard, C. Bedon, A. Baghlani, Damage evaluation of H-section steel columns under impulsive blast loads via gene expression programming, Eng. Struct. 219 (2020) 110909.

[93] M. Abedini, C. Zhang, J. Mehrmashhadi, E. Akhlaghi, Comparison of ALE, LBE and pressure time history methods to evaluate extreme loading effects in RC column, in: Proceedings of the Structures, 2020, pp. 456–466.

[94] B. Abdelwahed, Nonlinear numerical simulation for reinforced concrete elements with explicit time integration procedure, Case Stud. Constr. Mater. 12 (2020) e00344.

[95] Jr N.F. Knight, N. Jaunky, R.E. Lawson, D.R. Ambur, Penetration simulation for uncontained engine debris impact on fuselage-like panels using LS-DYNA, Finite Elem. Anal. Des. 36 (2000) 99–133.

[96] C.E.-I.d. Béton, CEB-FIP Model Code 1990: Design Code, Thomas Telford Publishing, 1993.

[97] H. Xu, H. Wen, Semi-empirical equations for the dynamic strength enhancement of concrete-like materials, Int. J. Impact Eng. 60 (2013) 76–81.

[98] L.J. Malvar, J.E. Crawford, Dynamic increase factors for concrete, DTIC document 1 (1.6) (1998).

[99] F. Fema 426, Reference Manual to Mitigate Potential Terrorist Attacks against Buildings-Buildings and Infrastructure Protection Series, 2003.

[100] M. Kennett, E. Letvin, M. Chipley, T. Ryan, FEMA 452-Risk Assessment, Federal Emergency Management Agency, 2005.

[101] H. Jia, L. Yu, G. Wu, Damage assessment of two-way bending RC slabs subjected to blast loadings, Sci. World J. 2014 (2014).

[102] M.A. Hadianfard, S. Malekpour, M. Momeni, Reliability analysis of H-section steel columns under blast loading, Struct. Saf. 75 (2018) 45–56.

[103] W.L. Bounds, Design of Blast-Resistant Buildings in Petrochemical Facilities, ASCE Publications, 2010.

[104] A. Johari, M. Momeni, Stochastic analysis of ground response using non-recursive algorithm, Soil Dynam. Earthq. Eng. 69 (2015) 57–82.

[105] A. Johari, M. Momeni, A. Javadi, An Analytical Solution for Reliability Assessment of Pseudo-static Stability of Rock Slopes Using Jointly Distributed Random Variables Method, 2015.